View metadata, citation and similar papers at core.ac.uk

brought to you by CORE

provided by The Australian National University

Mon. Not. R. Astron. Soc. **301,** 261–279 (1998)

X-ray properties of the Parkes sample of flat-spectrum radio sources: dust in radio-loud quasars?

J. Siebert,[1] W. Brinkmann,[1] M. J. Drinkwater,[2] W. Yuan,[1] P. J. Francis,[3] B. A. Peterson[3] and R. L. Webster[4]

[1] *Max-Planck-Institut für extraterrestrische Physik, Giessenbachstrasse, D-85740 Garching, Germany*
[2] *School of Physics, University of New South Wales, Sydney 2052, Australia*
[3] *Mt Stromlo & Siding Spring Observatories, Australian National University, Weston Creek, ACT 2611, Australia*
[4] *School of Physics, University of Melbourne, Parkville, Victoria 3052, Australia*

Accepted 1998 July 30. Received 1998 July 30; in original form 1997 December 22

ABSTRACT

We investigate the X-ray properties of the Parkes sample of flat-spectrum radio sources using data from the *ROSAT* All-Sky Survey and archival pointed PSPC observations. In total, 163 of the 323 sources are detected. For the remaining 160 sources, 2σ upper limits to the X-ray flux are derived. We present power-law photon indices in the 0.1–2.4 keV energy band for 115 sources, which were determined either with a hardness ratio technique or from direct fits to pointed PSPC data if a sufficient number of photons were available. The average photon index is $\langle\Gamma\rangle = 1.95^{+0.13}_{-0.12}$ for flat-spectrum radio-loud quasars, $\langle\Gamma\rangle = 1.70^{+0.23}_{-0.24}$ for galaxies, and $\langle\Gamma\rangle = 2.40^{+0.12}_{-0.31}$ for BL Lac objects. The soft X-ray photon index is correlated with redshift and with radio spectral index in the sense that sources at high redshift and/or with flat (or inverted) radio spectra have flatter X-ray spectra on average. The results are in accord with orientation-dependent unification schemes for radio-loud active galactic nuclei.

Webster et al. discovered many sources with unusually red optical continua among the quasars of this sample, and interpreted this result in terms of extinction by dust. Although the X-ray spectra in general do not show excess absorption, we find that low-redshift optically red quasars have significantly lower soft X-ray luminosities on average than objects with blue optical continua. The difference disappears for higher redshifts, as is expected for intrinsic absorption by cold gas associated with the dust. In addition, the scatter in $\log(f_x/f_o)$ is consistent with the observed optical extinction, contrary to previous claims based on optically or X-ray selected samples.

Although alternative explanations for the red optical continua cannot be excluded with the present X-ray data, we note that the observed X-ray properties are consistent with the idea that dust plays an important role in some of the radio-loud quasars with red optical continua.

Key words: dust, extinction – galaxies: active – quasars: general – X-rays: galaxies.

1 INTRODUCTION

Between 1990 August and 1991 February, *ROSAT* (Trümper 1982) performed a survey of the whole sky in the soft X-ray band between 0.1 and 2.4 keV (Voges 1992) with the Position Sensitive Proportional Counter (PSPC: Pfeffermann et al. 1987). This survey yielded about 60 000 X-ray sources with integrated fluxes greater than a few times 10^{-13} erg cm^{-2} s^{-1}. One of the outstanding achievements of this survey is that it offers the possibility to investigate the X-ray properties of large samples of astrophysical objects in an unbiased way.

Many well-defined samples of active galactic nuclei (AGN), selected from different wavebands, have meanwhile been studied in the X-ray regime: among others, the Large Bright Quasar Sample (LBQS: Green et al. 1995), the Molonglo quasar sample (Baker & Hunstead 1995), the 3CRR catalogue (Prieto 1996) and the Wall & Peacock 2-Jy sample (Siebert et al. 1996). In addition, the *ROSAT* All–Sky Survey (RASS) has been correlated with large radio catalogues like the Molonglo Reference Catalog (Large et al. 1981; Brinkmann, Siebert & Boller 1994) and the Green Bank 5-GHz survey (Condon, Broderick & Seielstad 1989; Brinkmann et al. 1995, 1997b), as well as the Véron quasar catalogue (Véron-Cetty & Véron 1993; Brinkmann, Yuan & Siebert 1997a; Yuan, Brinkmann & Siebert 1998). For the first time it is possible to compare the X-ray properties of large samples of AGN selected at different wavelengths. These studies make an important

© 1998 RAS

Downloaded from https://academic.oup.com/mnras/article-abstract/301/1/261/1058213 by Library user on 07 September 2018

contribution to our understanding of the phenomenological differences between the various types of AGN and the underlying physical processes.

In this paper we investigate the X-ray properties of the Parkes sample of flat-spectrum radio sources (Drinkwater et al. 1997). The choice of this sample was particularly motivated by the recent discovery of a large number of sources with extremely red optical to infrared continua in this sample (Webster et al. 1995). It was suggested that this reddening is due to dust in the line of sight, and it therefore seemed natural to look for the imprints of this material on the soft X-ray emission by absorption at very low energies.

Moreover, it is interesting to compare the X-ray properties of flat-spectrum quasars with those of steep-spectrum quasars, like, for example, the Molonglo quasar sample (Baker & Hunstead 1995) or the steep-spectrum quasars of Brinkmann et al. (1997a). Since orientation-based unification schemes for radio-loud quasars predict that both classes belong to the same parent population, but with different orientations to the line of sight, it is important to see how the X-ray properties fit into this scenario.

The outline of the paper is as follows. In Section 2 we introduce the Parkes catalogue of flat-spectrum radio sources, and describe the analysis of the X-ray data from the RASS and pointed PSPC observations in Section 3. Section 4 deals with the results of our analysis in terms of detection rates, variability, X-ray spectra and luminosity correlations. In Section 5 we focus on the X-ray evidence for dust-reddened quasars. A discussion of our results and the conclusions are presented in Sections 6 and 7, respectively.

2 THE CATALOGUE

The original Parkes catalogue contains about 10 000 radio sources and was the result of a survey of the southern sky with the Parkes radio telescope at 2.7 GHz between 1968 and 1979 (Bolton, Savage & Wright 1979; Wright & Otrupcek 1990). To compile a large and unbiased sample of radio-selected quasars, sources were selected from the original survey papers according to the following criteria (Drinkwater et al. 1997): $S_{2.7\,\mathrm{GHz}} > 0.5$ Jy, radio spectral index $\alpha_{2.7}^{5} > -0.5$ (where $S_\nu \propto \nu^\alpha$), Galactic latitude $|b| > 20°$, $-45° < \delta_{1950.0} < +10°$; 2.7-GHz ($S_{2.7\,\mathrm{GHz}}$) and 5-GHz ($S_{5\,\mathrm{GHz}}$) flux densities available in the papers.

By selecting flat-spectrum radio sources the resulting sample is biased towards core-dominated quasars, because radio galaxies and lobe-dominated quasars generally have steeper radio spectra. The final complete list contains 323 sources. Special care has been taken in the optical identification of the objects and in the determination of their redshifts. Using optical data bases and new observations, 321 sources could be identified and for 277 of them redshifts are available.

Drinkwater et al. (1997) used digitized optical plates to classify the morphologies automatically as 237 'stellar' (unresolved), 35 'galaxy' (resolved), 11 'merged' (two or more images too close together on the optical plate to be separated) and 38 'faint' sources (too faint to classify). They used CCD images to deconvolve and identify the 11 'merged' objects. All of these were 'stellar' except PKS 1555−140 which was a 'galaxy'. For the purposes of this paper we define an additional category of 14 'BL Lac objects' being the 12 'stellar' objects, one 'galaxy' and one 'merged' object that are bona fide BL Lac objects according to Padovani & Giommi (1995).[1] These objects will be handled separately in the following subsections. We divide the remaining sources as follows: 234 stellar sources ('quasars'), 35 'galaxies' and 38 'faint' sources. Note that the quasar/galaxy distinction is only based on morphology so that a quasar with an associated nebulosity like PKS 0445+097 is classified as a 'galaxy'. For a discussion of the completeness of the sample and a detailed presentation of the radio and optical data, see Drinkwater et al. (1997).

[1] In detail, the 14 BL Lac objects are 0048−097, 0118−272, 0138−097, 0301−243, 0422+004, 0426−380, 0537−441, 0823+033, 0829+046, 1144−379, 1514−241, 1519−273, 2131−021 and 2240−260.

3 DATA ANALYSIS

3.1 *ROSAT* All–Sky Survey data

For each of the sample sources a $1° \times 1°$ field centred on the radio position was extracted from the RASS and analysed using a procedure based on standard routines within the EXSAS environment (Zimmermann et al. 1994). This procedure uses a maximum-likelihood source detection algorithm which returns the likelihood of existence for a X-ray source at the specified radio position, the number of source photons within 5 times the FWHM of the PSPC point spread function, and the error in the number of source photons. For the RASS the FWHM of the PSPC point spread function is estimated to be ∼60 arcsec (Zimmermann et al. 1994).

The choice of the background has a significant influence on the results of the source detection procedure, in particular for weak sources. We estimated the local background by taking the average of two source free boxes, each 10 by 10 arcmin^2 in size, which are offset by 15 arcmin from the radio position along the scanning direction of the satellite during the RASS observations. In this way it is ensured that the background regions have an exposure similar to the source region.

Since it is known that an AGN is present at the position of the radio source, we considered a radio source to be detected in X-rays if the likelihood of existence is greater than 5.91, which corresponds to 3σ. If no X-ray source is detected above the specified significance level, we determined the 2σ upper limit on the number of X-ray photons. To calculate the corresponding count rates we used the vignetting-corrected RASS exposure averaged over a circle with radius 5 arcmin centred on the radio position.

The unabsorbed fluxes were calculated using the standard 'energy to counts conversion factors' (ECFs) assuming a simple power-law model modified by Galactic absorption. We used the photon indices[2] Γ listed in Tables 1 and 2, if the uncertainty was smaller than 0.5. For the other sources we applied $\Gamma = 2.0$ for quasars and $\Gamma = 1.7$ for galaxies. These values represent the average spectral indices of the respective object classes derived in Section 4.4.

3.2 Pointed *ROSAT* observations

In addition to the RASS data, we searched the *ROSAT* source catalogue (*ROSAT*-SRC: Voges et al. 1994), which was generated from pointed PSPC observations. We found 49 sources that were in the field of view of an observation either as the main target or serendipitously. Of these, 12 were detected in the pointed observation only. Fluxes and luminosities were calculated based on the count rates from the catalogue and assuming the same spectral parameters as for the RASS data. In the analysis we used the fluxes from the pointed observations only when no Survey detection was available.

[2] Γ is the power-law slope of the X-ray photon spectrum defined as $N(E) \propto E^{-\Gamma}$. It is connected to the energy index via $\alpha = \Gamma - 1$.

Downloaded from https://academic.oup.com/mnras/article-abstract/301/1/261/1058213 by Library user on 07 September 2018

Table 1. X-ray properties of the Parkes sample of flat-spectrum radio sources.

Object (1)	Type (2)	m_B (3)	z (4)	$f_{2.7GHz}$ (5)	(6)	count s^{-1} (7)	F_x (8)	$N_{H,gal}$ (9)	Γ_{gal} (10)	$N_{H,free}$ (11)	Γ_{free} (12)	(13)
0003−066	s	18.5	0.347	1.460	S	0.070± 0.016	1.300± 0.305	3.14	$1.58^{+0.48}_{-0.92}$	...	...	
0005−239	s	16.6	1.407	0.580	S	<0.018	< 0.278	2.29	...	...	...	
0005−262	s	0.0	0.000	0.580	S	<0.011	< 0.145	1.74	...	...	...	
0008−264	s	19.5	1.096	0.670	S	<0.013	< 0.196	2.19	...	...	...	
0013−005	s	19.4	1.574	0.890	S	<0.019	< 0.333	2.91	...	...	...	
0036−216	g	21.0	0.000	0.530	S	<0.014	< 0.191	1.56	...	...	...	
0038−020	s	18.8	1.178	0.610	S	<0.019	< 0.337	2.83	...	...	...	
0048−097	s	16.8	0.000	1.440	SP	0.197± 0.021	5.130± 0.537	3.52	$2.70^{+0.15}_{-0.16}$	$2.04^{+2.93}_{-1.93}$	$2.15^{+1.04}_{-0.96}$	*
0048−071	f	22.1	1.974	0.700	S	<0.014	< 0.339	5.38	...	...	...	
0048−427	s	20.0	1.749	0.680	S	0.019± 0.008	0.428± 0.189	4.63	...	...	...	
0056−001	s	17.8	0.717	1.800	S	0.045± 0.014	0.972± 0.297	3.06	$2.40^{+0.47}_{-0.52}$	...	...	
0104−408	s	18.9	0.584	0.570	S	0.046± 0.013	0.842± 0.234	3.04	$1.78^{+0.50}_{-0.72}$	$1.57^{+11.82}_{-1.45}$	$1.32^{+2.42}_{-1.30}$	
0106+013	s	18.8	2.094	1.880	S	0.021± 0.010	0.372± 0.176	2.78	$2.41^{+0.69}_{-0.73}$	$1.83^{+15.65}_{-1.72}$	$2.05^{+3.93}_{-1.77}$	
0108−079	s	18.5	1.773	1.020	S	<0.012	< 0.284	5.17	...	...	...	
0111+021	g	16.4	0.047	0.610	S	0.059± 0.014	1.040± 0.242	3.15	...	...	...	
0112−017	s	17.9	1.381	1.380	S	0.047± 0.013	1.050± 0.278	4.49	$1.81^{+0.58}_{-0.88}$	$4.99^{+31.90}_{-4.86}$	$1.92^{+3.88}_{-1.89}$	
0113−118	s	19.4	0.672	1.780	S	0.087± 0.031	1.680± 0.599	3.38	$1.79^{+0.73}_{-1.49}$	$11.42^{+1.21}_{-11.19}$	$4.05^{+1.84}_{-2.69}$	
0114+074	g	22.1	0.343	0.900	S	0.028± 0.010	0.544± 0.193	4.05	...	...	...	
(0115−016)	X	0.0	0.000	0.640	S	<0.012	< 0.237	3.52	...	...	...	
0116−219	s	19.6	1.161	0.570	S	0.016± 0.008	0.200± 0.096	1.46	...	...	...	
0116+082	s	21.9	0.594	1.500	S	0.013± 0.006	0.279± 0.132	4.10	...	...	...	
0118−272	s	17.5	0.556	0.960	SP	0.081± 0.017	1.050± 0.217	1.53	...	...	...	*
0119+041	s	19.2	0.637	1.830	S	0.036± 0.011	0.690± 0.209	3.37	$1.86^{+0.50}_{-0.66}$	$15.81^{+18.25}_{-12.61}$	$4.67^{+1.30}_{-3.01}$	
0122−003	s	16.5	1.080	1.430	SP	0.078± 0.015	1.630± 0.308	3.36	$2.46^{+0.30}_{-0.33}$	$3.08^{+6.60}_{-2.98}$	$2.35^{+2.07}_{-1.51}$	*
(0123−016)	D	13.0	0.018	2.170	SP	0.039± 0.011	0.770± 0.227	3.56	...	...	...	
0130−171	s	17.6	1.022	0.990	S	0.030± 0.010	0.370± 0.129	1.42	$2.15^{+0.47}_{-0.44}$	...	...	
0130−447	f	0.0	0.000	0.590	S	<0.025	< 0.324	1.51	...	...	...	
0131−001	f	0.0	0.879	0.680	S	<0.011	< 0.191	2.92	...	...	...	
0133−204	s	18.2	1.141	0.680	S	0.039± 0.014	0.488± 0.173	1.40	$2.45^{+0.62}_{-0.48}$	$4.27^{+9.32}_{-4.17}$	$3.58^{+2.39}_{-2.35}$	
0135−247	s	18.9	0.829	1.370	SP	0.166± 0.031	2.020± 0.371	1.38	$2.79^{+0.37}_{-0.29}$	$1.11^{+8.74}_{-1.00}$	$2.64^{+3.35}_{-0.91}$	*
0137+012	g	19.4	0.260	1.070	SP	0.151± 0.026	2.780± 0.473	3.06	$2.31^{+0.27}_{-0.27}$	$1.17^{+4.92}_{-1.06}$	$1.61^{+1.71}_{-0.80}$	*
0138−097	s	18.5	0.501	0.710	S	0.032± 0.010	0.683± 0.214	2.84	...	...	...	
0142−278	s	17.5	1.153	0.820	S	<0.023	< 0.311	1.63	...	...	...	
0146+056	s	20.7	2.345	0.720	S	<0.011	< 0.243	4.45	...	...	...	
0150−334	s	17.4	0.610	0.920	S	0.048± 0.012	0.630± 0.158	1.58	$0.61^{+0.47}_{-0.61}$	$1.65^{+48.53}_{-1.50}$	$0.63^{+4.64}_{-0.34}$	
0153−410	g	19.4	0.226	1.220	S	<0.006	< 0.082	1.71	...	...	...	
(0156−144)	X	0.0	0.000	0.900	S	<0.010	< 0.118	1.38	...	...	...	
0202−172	s	18.2	1.740	1.400	S	0.063± 0.016	0.956± 0.246	2.09	$1.30^{+0.46}_{-0.65}$	$6.58^{+27.39}_{-6.46}$	$2.53^{+3.41}_{-2.50}$	
0213−026	f	0.0	1.178	0.500	S	0.017± 0.009	0.291± 0.149	2.59	...	...	...	
(0215+015)	B	18.5	0.000	0.730	S	<0.016	< 0.312	3.60	...	...	...	
0216+011	f	21.8	1.610	0.500	S	<0.013	< 0.230	3.05	...	...	...	
0220−349	f	21.5	1.490	0.600	S	<0.009	< 0.137	1.91	...	...	...	
0221+067	s	20.8	0.510	0.790	S	0.068± 0.020	1.700± 0.504	5.94	...	...	...	
0226−038	s	17.6	2.066	0.660	S	0.068± 0.022	1.100± 0.351	2.35	$1.82^{+0.58}_{-0.79}$	$6.99^{+32.30}_{-6.79}$	$3.34^{+2.58}_{-3.23}$	
0229−398	s	22.3	1.646	0.640	S	<0.009	< 0.147	2.25	...	...	...	
0232−042	s	16.2	1.437	0.840	SP	0.124± 0.035	2.270± 0.633	2.59	$2.08^{+0.40}_{-0.45}$	$3.32^{+10.29}_{-3.19}$	$2.33^{+3.11}_{-1.79}$	*
0237+040	s	18.5	0.978	0.730	S	<0.044	< 1.070	5.47	...	...	...	
(0237−027)	Q	19.0	0.000	0.680	S	<0.023	< 0.413	2.87	...	...	...	
0238−084	g	11.7	0.005	0.580	SP	0.033± 0.014	0.564± 0.241	3.08	...	...	...	*
0240−217	g	19.0	0.314	0.970	S	0.228± 0.029	3.780± 0.482	2.76	$1.12^{+0.25}_{-0.29}$	$10.45^{+40.13}_{-5.87}$	$2.81^{+3.04}_{-1.28}$	
0240−060	s	18.2	1.800	0.530	S	<0.018	< 0.316	2.86	...	...	...	
0256+075	s	18.9	0.895	0.690	UP	0.010± 0.002	0.313± 0.062	11.83	$1.24^{+1.00}_{-1.00}$	$3.61^{+37.73}_{-3.49}$	$0.70^{+4.14}_{-0.17}$	
0301−243	s	16.4	0.000	0.520	SP	0.645± 0.051	9.990± 0.796	1.74	$2.89^{+0.15}_{-0.14}$	$1.49^{+3.07}_{-1.38}$	$2.76^{+1.27}_{-0.87}$	*
0316−444	g	14.9	0.076	0.820	SP	2.280± 0.105	37.600± 1.730	2.53	$1.86^{+0.10}_{-0.10}$	$3.60^{+2.11}_{-1.88}$	$2.22^{+0.67}_{-0.66}$	*
0320+015	-	0.0	0.000	0.520	S	<0.007	< 0.207	8.05	...	...	...	
0327−241	s	19.4	0.888	0.630	S	<0.025	< 0.325	1.55	...	...	...	
0332+078	f	0.0	0.000	0.740	S	<0.011	< 0.419	17.10	...	...	...	
0332−403	s	16.8	1.445	1.960	S	0.082± 0.024	1.020± 0.304	1.43	...	...	...	
0336−017	s	20.1	3.202	0.580	S	<0.012	< 0.338	7.70	...	...	...	
0336−019	s	18.4	0.850	2.230	S	0.057± 0.014	1.570± 0.380	7.70	...	...	...	
0338−214	s	16.0	0.048	0.820	S	0.017± 0.008	0.297± 0.141	2.79	...	...	...	
0346−163	s	17.4	0.000	0.540	S	<0.007	< 0.153	4.05	...	...	...	

Downloaded from https://academic.oup.com/mnras/article-abstract/301/1/261/1058213 by Library user on 07 September 2018

Table 1 – *continued*

Object (1)	Type (2)	m_B (3)	z (4)	$f_{2.7GHz}$ (5)	(6)	count s^{-1} (7)	F_x (8)	$N_{H,gal}$ (9)	Γ_{gal} (10)	$N_{H,free}$ (11)	Γ_{free} (12)	(13)
0346−279	s	20.5	0.987	1.100	S	0.132± 0.025	1.290± 0.241	0.96	$2.55^{+0.35}_{-0.28}$	$1.91^{+8.46}_{-1.80}$	$3.00^{+3.00}_{-1.28}$	
0348+049	f	0.0	0.000	0.540	S	<0.009	< 0.293	13.29	...	...	...	
0348−120	s	17.9	1.520	0.500	S	<0.009	< 0.172	3.45	...	...	...	
0349−278	g	16.8	0.066	2.890	S	<0.013	< 0.144	0.99	...	...	...	
0357−264	s	21.8	1.470	0.580	S	<0.007	< 0.091	1.79	...	...	...	
0400−319	s	20.2	1.288	1.140	S	<0.017	< 0.181	1.01	...	...	...	
0402−362	s	17.0	1.417	1.040	S	0.226± 0.024	2.180± 0.231	0.76	$1.83^{+0.14}_{-0.14}$	$1.34^{+3.06}_{-1.24}$	$2.09^{+1.18}_{-0.76}$	
0403−132	s	16.8	0.571	3.150	SP	0.083± 0.017	1.540± 0.320	3.57	$0.81^{+0.63}_{-0.81}$	...	...	*
0405−385	g	19.8	1.285	1.020	S	0.033± 0.013	0.404± 0.157	1.24	...	...	...	
0405−123	s	14.4	0.574	2.350	SP	0.419± 0.036	10.500± 0.904	3.87	$2.35^{+0.14}_{-0.15}$	$4.50^{+3.09}_{-2.64}$	$2.55^{+0.94}_{-0.91}$	*
0405−331	s	19.4	2.562	0.700	S	<0.017	< 0.193	1.14	...	...	...	
0406−311	g	16.0	0.056	0.550	S	<0.026	< 0.366	1.75	...	...	...	
0406−127	s	18.0	1.563	0.590	S	<0.013	< 0.275	3.80	...	...	...	
0407−170	f	0.0	0.000	0.550	S	<0.010	< 0.173	2.49	...	...	...	
0414−189	s	19.4	1.536	1.180	S	<0.015	< 0.250	2.67	...	...	...	
0413−210	s	18.6	0.808	1.790	S	0.046± 0.013	0.733± 0.214	2.31	$1.12^{+0.72}_{-1.12}$	$3.98^{+31.05}_{-3.88}$	$1.48^{+4.47}_{-0.29}$	
0420−014	s	17.4	0.914	1.920	S	0.105± 0.022	2.980± 0.622	8.23	$1.83^{+0.60}_{-0.91}$	$6.81^{+49.15}_{-6.68}$	$1.63^{+4.10}_{-1.62}$	
0422+004	s	16.2	0.000	1.250	S	0.049± 0.015	1.980± 0.622	7.06	...	...	...	
0421+019	s	17.1	2.055	0.760	S	<0.022	< 0.715	11.31	...	...	...	
0423−163	f	0.0	0.000	0.550	S	<0.008	< 0.152	3.12	...	...	...	
0423+051	g	19.2	1.333	0.610	S	<0.014	< 0.389	11.60	...	...	...	
0426−380	s	18.4	1.030	1.040	S	0.028± 0.011	0.408± 0.155	1.98	...	...	...	*
0430+052	g	12.9	0.033	3.300	SP	1.710± 0.154	50.300± 4.530	10.79	$1.75^{+0.28}_{-0.31}$	...	...	*
0434−188	s	18.7	2.705	1.050	S	<0.017	< 0.305	2.77	...	...	...	
0438−436	s	19.1	2.852	6.500	SP	0.045± 0.014	0.701± 0.212	1.47	...	...	...	*
0440−003	s	18.2	0.844	3.530	S	0.057± 0.016	1.450± 0.407	6.09	...	...	...	
0445+097	g	20.2	2.115	0.680	S	0.027± 0.010	0.789± 0.295	14.07	...	...	...	
0448−392	s	16.8	1.288	0.890	S	0.105± 0.027	1.520± 0.391	1.90	$1.95^{+0.38}_{-0.42}$	...	...	
0451−282	s	17.8	2.564	2.380	S	0.024± 0.009	0.379± 0.147	2.21	$1.81^{+0.48}_{-0.59}$	$9.83^{+30.23}_{-9.73}$	$4.08^{+1.87}_{-3.40}$	
0454+066	s	19.8	0.405	0.500	S	<0.023	< 0.677	8.66	...	...	...	
0454−234	s	18.2	1.003	1.760	S	<0.010	< 0.179	2.93	...	...	...	
0456+060	f	0.0	0.000	0.780	S	<0.014	< 0.411	8.66	...	...	...	
0457+024	s	18.2	2.382	1.630	S	<0.014	< 0.394	8.01	...	...	...	
0458−020	s	19.1	2.310	1.990	S	<0.017	< 0.480	7.98	...	...	...	
0459+060	s	19.7	1.106	0.990	S	<0.012	< 0.355	9.42	...	...	...	
0500+019	f	0.0	0.000	2.470	UP	0.012± 0.001	0.326± 0.026	7.98	...	...	...	*
0502+049	s	18.7	0.954	0.590	S	0.031± 0.011	0.998± 0.347	11.27	...	...	...	
0508−220	g	16.9	0.172	0.900	S	<0.018	< 0.283	2.54	...	...	...	
0511−220	g	20.2	0.000	1.210	S	0.025± 0.010	0.400± 0.162	2.54	...	...	...	
0514−161	s	16.9	1.278	0.800	S	0.017± 0.009	0.424± 0.228	6.22	$3.30^{+0.70}_{-0.82}$	$13.91^{+26.18}_{-13.06}$	$5.46^{+0.51}_{-4.14}$	
0521−365	g	16.7	0.055	12.500	SP	1.020± 0.043	19.200± 0.809	3.29	$1.34^{+0.19}_{-0.21}$	$5.74^{+4.48}_{-3.30}$	$1.98^{+0.93}_{-0.93}$	
0528−250	s	17.7	2.765	1.320	S	<0.022	< 0.339	2.18	...	...	...	
0532−378	s	21.4	1.668	0.700	S	0.015± 0.007	0.260± 0.117	2.67	...	...	...	
0533−120	g	18.6	0.157	0.800	S	<0.017	< 0.476	11.67	...	...	...	
0537−441	s	15.4	0.894	3.840	SP	0.154± 0.018	4.460± 0.507	4.11	$2.45^{+0.15}_{-0.17}$	$3.35^{+2.94}_{-2.42}$	$2.20^{+0.92}_{-0.91}$	*
0537−158	s	16.5	0.947	0.630	S	0.048± 0.012	1.280± 0.308	6.90	$1.92^{+0.79}_{-1.22}$	$2.30^{+38.03}_{-2.19}$	$1.13^{+3.88}_{-1.11}$	
0537−286	s	19.3	3.110	0.740	SP	0.072± 0.014	1.090± 0.212	2.06	$1.00^{+0.27}_{-0.36}$	$12.89^{+38.94}_{-7.82}$	$3.42^{+2.51}_{-1.66}$	*
0622−441	s	18.6	0.688	0.770	S	0.046± 0.009	2.390± 0.480	5.90	$2.92^{+0.35}_{-0.43}$	$2.36^{+6.07}_{-2.26}$	$1.83^{+1.86}_{-1.29}$	
0629−418	s	18.1	1.416	0.530	S	<0.026	< 0.673	6.39	...	...	...	
0823+033	s	0.0	0.506	0.870	S	0.100± 0.020	2.490± 0.509	3.49	$1.52^{+0.32}_{-0.44}$	$1.20^{+5.95}_{-1.07}$	$0.81^{+1.70}_{-0.78}$	
0829+046	s	16.0	0.000	0.620	S	0.041± 0.015	0.943± 0.343	3.13	...	...	...	
0837+035	s	20.4	1.570	0.690	S	<0.011	< 0.218	3.61	...	...	...	
0859−140	s	16.3	1.335	2.930	S	0.037± 0.013	0.919± 0.312	5.78	$2.23^{+0.61}_{-1.16}$	$0.59^{+10.05}_{-0.49}$	$0.77^{+2.45}_{-0.76}$	
0906+015	s	17.2	1.018	1.200	S	0.053± 0.015	1.260± 0.350	3.26	$2.50^{+0.41}_{-0.44}$	...	...	
0907−023	s	19.1	0.957	0.570	S	<0.008	< 0.137	2.88	...	...	...	
0912+029	s	19.6	0.427	0.540	S	<0.025	< 0.488	3.32	...	...	...	
0921−213	g	16.4	0.052	0.530	S	0.356± 0.030	7.540± 0.635	5.09	$1.86^{+0.20}_{-0.25}$	$8.34^{+6.13}_{-4.22}$	$2.65^{+1.18}_{-1.10}$	
0922+005	s	17.3	1.717	0.740	S	<0.013	< 0.256	3.38	...	...	...	
0925−203	s	16.4	0.348	0.810	S	0.167± 0.021	3.700± 0.463	3.71	$2.17^{+0.18}_{-0.20}$	$3.62^{+3.39}_{-2.78}$	$2.14^{+1.02}_{-1.01}$	
1004−018	s	20.3	1.212	0.560	S	<0.013	< 0.260	3.70	...	...	...	

Downloaded from https://academic.oup.com/mnras/article-abstract/301/1/261/1058213 by Library user on 07 September 2018

Table 1 – *continued*

Object (1)	Type (2)	m_B (3)	z (4)	$f_{2.7GHz}$ (5)	(6)	count s^{-1} (7)	F_x (8)	$N_{H,gal}$ (9)	Γ_{gal} (10)	$N_{H,free}$ (11)	Γ_{free} (12)	(13)
1008−017	s	19.6	0.406	0.800	S	<0.026	< 0.527	3.70	...	...	...	
1016−311	s	17.6	0.794	0.620	S	<0.016	< 0.380	5.07	...	...	...	
1020−103	s	15.1	0.197	0.640	S	0.182± 0.023	3.830± 0.479	4.84	$1.74^{+0.24}_{-0.30}$	$3.48^{+4.14}_{-3.09}$	$1.40^{+1.00}_{-1.04}$	
1021−006	s	17.9	2.547	0.950	S	<0.008	< 0.168	4.56	...	...	...	
1032−199	s	18.3	2.189	1.100	S	<0.017	< 0.418	5.43	...	...	...	
1034−293	s	15.9	0.312	1.330	SP	0.064± 0.016	1.390± 0.348	4.07	$2.49^{+0.37}_{-0.41}$	$8.37^{+10.98}_{-6.82}$	$3.75^{+2.25}_{-2.20}$	*
1036−154	s	21.8	0.525	0.750	S	<0.016	< 0.374	5.41	...	...	...	
1038+064	s	16.1	1.270	1.740	S	0.086± 0.017	1.500± 0.293	2.70	...	...	...	
1042+071	s	18.5	0.698	0.500	S	<0.017	< 0.295	2.66	...	...	...	
1045−188	s	18.4	0.595	0.940	S	0.054± 0.015	1.860± 0.508	3.97	$2.85^{+0.44}_{-0.45}$	$1.70^{+8.53}_{-1.58}$	$2.04^{+2.83}_{-1.23}$	
1048−313	s	18.5	1.429	0.800	S	<0.008	< 0.209	5.98	...	...	...	
1055−243	s	19.9	1.086	0.770	S	<0.014	< 0.365	6.32	...	...	...	
1055+018	s	18.5	0.888	3.020	SP	0.068± 0.016	1.740± 0.398	3.96	$2.35^{+0.34}_{-0.40}$	...	...	*
1101−325	s	16.5	0.355	0.930	S	0.131± 0.021	3.250± 0.527	6.65	$1.85^{+0.38}_{-0.50}$	$12.09^{+38.36}_{-8.27}$	$2.72^{+2.98}_{-1.65}$	
1102−242	s	20.6	1.666	0.500	S	<0.016	< 0.387	5.81	...	...	...	
(1103−006)	Q	15.4	0.427	0.590	S	0.068± 0.015	2.390± 0.539	4.67	$2.69^{+0.39}_{-0.43}$	$5.05^{+8.79}_{-4.95}$	$2.80^{+2.53}_{-2.08}$	
1106+023	g	18.0	0.157	0.640	S	0.026± 0.011	0.507± 0.218	4.23	...	...	...	
1107−187	f	0.0	0.497	0.650	S	<0.011	< 0.236	4.44	...	...	...	
1110−217	f	0.0	0.000	0.940	S	<0.011	< 0.211	3.50	...	...	...	
1115−122	s	18.1	1.739	0.670	S	<0.018	< 0.425	5.22	...	...	...	
1118−056	s	19.0	1.297	0.660	S	0.026± 0.011	0.536± 0.225	3.99	...	...	...	
1124−186	s	18.6	1.050	0.610	S	0.462± 0.039	10.800± 0.901	4.04	$2.28^{+0.15}_{-0.16}$	$3.39^{+3.01}_{-2.50}$	$2.08^{+0.92}_{-0.92}$	
1127−145	s	17.0	1.184	5.970	S	0.069± 0.018	1.460± 0.377	4.06	$0.97^{+0.44}_{-0.65}$	$8.43^{+41.75}_{-8.07}$	$1.73^{+3.84}_{-1.73}$	
1128−047	f	21.4	0.266	0.740	S	<0.020	< 0.429	4.11	...	...	...	
1133−172	f	22.4	1.024	0.650	S	<0.007	< 0.133	3.68	...	...	...	
1136−135	s	16.3	0.557	2.760	S	0.127± 0.021	3.050± 0.514	3.66	$2.04^{+0.28}_{-0.34}$	$0.18^{+4.22}_{-0.07}$	$0.79^{+1.52}_{-0.42}$	*
1142+052	s	19.8	1.342	0.600	S	<0.025	< 0.406	2.41	...	...	...	
1142−225	f	0.0	0.000	0.540	S	<0.015	< 0.328	4.23	...	...	...	
1143−245	s	17.7	1.940	1.320	S	<0.010	< 0.241	5.17	...	...	...	
1145−071	s	19.0	1.342	1.090	UP	0.017± 0.009	0.343± 0.175	3.54	...	...	...	*
1144−379	s	18.4	1.048	1.070	SP	0.046± 0.023	2.160± 1.060	8.67	...	...	...	*
1148−001	s	17.1	1.980	2.560	S	0.052± 0.014	0.822± 0.221	2.26	$2.00^{+0.37}_{-0.39}$	$14.65^{+11.83}_{-8.70}$	$5.51^{+0.48}_{-2.42}$	
1148−171	s	17.9	1.751	0.600	S	<0.008	< 0.157	3.42	...	...	...	
1156−094	f	22.6	0.000	0.750	S	<0.014	< 0.273	3.58	...	...	...	
1156−221	s	18.6	0.565	0.710	S	<0.025	< 0.519	4.05	...	...	...	
1200−051	s	16.4	0.381	0.500	S	0.263± 0.030	5.030± 0.578	2.74	$2.29^{+0.15}_{-0.16}$	$1.50^{+3.10}_{-1.38}$	$1.81^{+1.12}_{-0.79}$	
(1201−041)	E	18.0	0.000	1.320	S	<0.010	< 0.183	2.83	...	...	...	
1202−262	s	19.8	0.789	1.340	S	0.031± 0.015	0.834± 0.390	7.01	...	...	...	
1206−399	s	17.2	0.966	0.590	S	<0.026	< 0.720	7.52	...	...	...	
1213−172	-	0.0	0.000	1.330	S	<0.081	< 1.740	4.21	...	...	...	
(1217+023)	Q	16.5	0.240	0.510	S	0.319± 0.032	4.800± 0.483	1.88	$2.38^{+0.17}_{-0.17}$	$1.56^{+3.57}_{-1.45}$	$2.24^{+1.35}_{-0.87}$	
1218−024	s	20.2	0.665	0.540	S	<0.026	< 0.453	2.80	...	...	...	
1222+037	s	19.3	0.957	0.810	S	0.043± 0.014	0.593± 0.199	1.69	$1.56^{+0.36}_{-0.46}$	...	...	
1226+023	s	12.9	0.158	43.400	SP	7.680± 0.146	110.000± 2.100	1.79	$2.19^{+0.08}_{-0.09}$	$0.70^{+1.42}_{-0.59}$	$1.71^{+0.62}_{-0.40}$	*
1228−113	f	22.0	0.000	0.550	S	0.028± 0.015	0.550± 0.296	3.49	...	...	...	
1229−021	s	16.6	1.045	1.330	S	<0.033	< 0.525	2.27	...	...	...	
1236+077	s	19.1	0.400	0.590	S	0.038± 0.013	0.532± 0.178	1.76	$1.99^{+0.37}_{-0.39}$	$4.92^{+10.53}_{-4.77}$	$3.09^{+2.91}_{-2.20}$	
1237−101	s	17.5	0.751	1.350	S	<0.026	< 0.486	3.26	...	...	...	
1243−072	s	17.6	1.286	0.790	S	0.042± 0.014	0.682± 0.226	2.38	$2.00^{+0.48}_{-0.52}$	...	...	
1244−255	s	16.2	0.638	1.340	S	0.087± 0.019	2.310± 0.504	6.96	$2.30^{+0.45}_{-0.63}$	$11.97^{+27.34}_{-9.10}$	$3.22^{+2.78}_{-2.12}$	
1250−330	s	21.4	0.000	0.520	S	0.018± 0.010	0.425± 0.241	5.14	...	...	...	
1253−055	s	17.7	0.540	12.000	SP	1.980± 0.085	31.100± 1.330	2.26	$1.66^{+0.11}_{-0.10}$	$2.53^{+1.81}_{-1.58}$	$1.75^{+0.59}_{-0.59}$	*
1255−316	s	18.5	1.924	1.490	S	<0.020	< 0.506	5.95	...	...	...	
1254−333	s	17.0	0.190	0.720	S	0.044± 0.015	1.080± 0.358	5.54	$1.88^{+0.61}_{-0.95}$	$11.35^{+14.55}_{-11.25}$	$2.87^{+3.09}_{-2.83}$	
1256−220	s	19.6	1.306	0.650	S	<0.017	< 0.459	7.09	...	...	...	
1256−229	s	16.7	1.365	0.500	S	<0.012	< 0.340	8.02	...	...	...	
1258−321	g	13.1	0.017	0.920	UP	0.030± 0.001	0.655± 0.032	5.40	$1.30^{+0.10}_{-0.12}$	...	...	
(1302−034)	Q	19.4	1.250	0.600	S	<0.016	< 0.235	1.96	...	...	...	
1302−102	s	15.7	0.286	0.890	SP	0.323± 0.036	7.350± 0.816	3.38	$2.62^{+0.17}_{-0.18}$	$2.85^{+3.41}_{-2.59}$	$2.42^{+1.15}_{-1.10}$	*
1313−333	s	16.8	1.210	1.000	S	<0.020	< 0.453	4.84	...	...	...	

Downloaded from https://academic.oup.com/mnras/article-abstract/301/1/261/1058213 by Library user on 07 September 2018

Table 1 – *continued*

Object (1)	Type (2)	m_B (3)	z (4)	$f_{2.7GHz}$ (5)	(6)	count s^{-1} (7)	F_x (8)	$N_{H,gal}$ (9)	Γ_{gal} (10)	$N_{H,free}$ (11)	Γ_{free} (12)	(13)
1317+019	s	20.8	1.232	0.550	UP	0.021± 0.003	0.314± 0.039	1.95	$1.64^{+0.20}_{-0.22}$	$3.05^{+3.90}_{-2.95}$	$2.01^{+1.18}_{-1.17}$	
1318−263	s	20.4	2.027	0.650	S	<0.015	< 0.381	6.36	...	...	...	
1327−311	s	18.5	1.335	0.520	S	<0.013	< 0.255	3.63	...	...	...	
1330+022	g	19.4	0.216	1.910	SP	0.216± 0.030	3.000± 0.412	1.76	$1.91^{+0.17}_{-0.18}$	$0.54^{+3.26}_{-0.43}$	$1.39^{+1.27}_{-0.44}$	*
1333−082	g	13.6	0.023	0.500	UP	0.022± 0.004	0.339± 0.063	2.28	$2.41^{+0.48}_{-0.45}$	$8.77^{+33.89}_{-5.71}$	$3.74^{+2.17}_{-1.34}$	
1334−127	s	15.7	0.539	2.010	SP	0.121± 0.021	2.540± 0.443	4.81	$1.99^{+0.30}_{-0.39}$	$6.61^{+9.28}_{-5.15}$	$2.44^{+1.62}_{-1.53}$	*
1336−260	s	20.1	1.510	0.710	S	<0.012	< 0.286	5.28	...	...	...	
1340−175	f	0.0	0.000	0.760	S	<0.018	< 0.506	8.01	...	...	...	
1349−145	f	0.0	0.000	1.040	S	0.018± 0.008	0.465± 0.215	6.42	...	...	...	
1351−018	s	21.3	3.709	0.980	SP	0.021± 0.010	0.412± 0.198	3.53	$2.28^{+0.56}_{-0.70}$	$2.63^{+14.33}_{-2.48}$	$1.98^{+4.02}_{-1.87}$	*
1352−104	s	17.6	0.332	0.790	S	0.137± 0.022	2.680± 0.438	3.42	$1.96^{+0.25}_{-0.29}$	$3.57^{+5.16}_{-3.45}$	$2.00^{+1.47}_{-1.42}$	
1353−341	g	18.6	0.223	0.640	S	0.039± 0.015	0.834± 0.317	5.15	$0.96^{+1.12}_{-0.96}$	$0.68^{+39.57}_{-0.51}$	$0.24^{+4.83}_{-0.24}$	
(1354−152)	Q	18.5	1.885	1.650	S	<0.023	< 0.622	7.22	...	...	...	
1354−174	s	17.9	3.137	1.280	S	<0.020	< 0.559	7.46	...	...	...	
(1356+022)	Q	18.3	1.329	0.750	S	0.029± 0.012	0.453± 0.182	2.26	...	...	...	
1359−281	s	18.7	0.803	0.820	S	<0.034	< 0.751	4.41	...	...	...	
1402−012	s	16.8	2.522	0.710	S	<0.008	< 0.175	4.06	...	...	...	
1402+044	s	21.3	3.211	0.580	UP	0.013± 0.002	0.198± 0.030	2.19	$1.60^{+0.23}_{-0.24}$	$9.34^{+7.16}_{-4.99}$	$3.65^{+1.59}_{-1.40}$	
1403−085	s	18.6	1.758	0.710	S	0.019± 0.010	0.333± 0.180	2.91	...	...	...	
1404−267	g	13.6	0.022	0.500	S	0.817± 0.054	14.800± 0.969	4.26	$1.11^{+0.14}_{-0.14}$	$16.50^{+31.49}_{-6.03}$	$3.27^{+2.63}_{-0.85}$	
1404−342	s	17.7	1.122	0.670	S	<0.025	< 0.616	5.49	...	...	...	
1406−076	s	20.3	1.494	0.960	S	<0.014	< 0.235	2.73	...	...	...	
1406−267	s	21.8	0.000	0.570	S	<0.020	< 0.459	4.78	...	...	...	
1411+094	g	19.7	0.162	0.600	S	<0.019	< 0.272	1.93	...	...	...	
1417−192	g	17.8	0.119	1.100	S	0.336± 0.034	13.200± 1.350	7.43	$2.70^{+0.20}_{-0.24}$	$8.85^{+4.84}_{-3.70}$	$3.05^{+1.06}_{-0.99}$	
1425−274	s	18.1	1.082	0.550	S	<0.020	< 0.485	5.35	...	...	...	
1430−178	s	17.8	2.326	1.000	S	<0.025	< 0.670	7.28	...	...	...	
1430−155	f	0.0	0.000	0.550	S	0.035± 0.016	0.973± 0.449	7.83	...	...	...	
1435−218	s	17.4	1.187	0.790	S	<0.013	< 0.349	7.53	...	...	...	
1437−153	s	19.9	0.000	0.720	S	<0.027	< 0.741	7.88	...	...	...	
1438−347	s	17.6	1.159	0.500	S	<0.025	< 0.594	5.44	...	...	...	
1443−162	s	20.5	0.000	0.780	S	<0.010	< 0.283	7.96	...	...	...	
1445−161	s	20.4	2.417	1.060	S	<0.038	< 1.070	8.08	...	...	...	
1450−338	f	0.0	0.000	0.720	S	<0.013	< 0.338	6.52	...	...	...	
(1451−400)	Q	18.5	1.810	0.710	S	<0.012	< 0.300	6.30	...	...	...	
1454−060	s	18.3	1.249	0.830	S	<0.010	< 0.261	6.28	...	...	...	
1456+044	s	20.1	0.394	0.680	S	0.066± 0.021	1.300± 0.405	3.50	...	...	...	
1504−166	s	19.0	0.876	2.300	S	<0.013	< 0.358	7.88	...	...	...	
1508−055	s	17.1	1.185	2.900	S	<0.042	< 1.130	6.92	...	...	...	
1509+022	g	19.8	0.219	0.690	S	0.050± 0.014	0.955± 0.268	3.92	$1.94^{+0.40}_{-0.55}$	$0.99^{+7.57}_{-0.86}$	$1.00^{+2.24}_{-0.98}$	
1510−089	s	16.2	0.362	2.800	UP	0.189± 0.006	5.260± 0.173	8.18	...	...	...	*
1511−100	s	17.6	1.513	0.560	S	<0.036	< 1.040	8.79	...	...	...	
1511−210	s	21.9	1.179	0.550	S	<0.011	< 0.320	8.36	...	...	...	
1514−241	g	16.4	0.049	2.000	S	0.052± 0.015	2.370± 0.687	8.80	...	...	...	
1518+045	g	12.8	0.052	0.500	S	<0.018	< 0.329	3.59	...	...	...	
1519−273	s	18.0	0.000	1.990	SP	0.034± 0.012	1.040± 0.364	8.90	...	...	...	*
1532+016	s	19.0	1.435	1.080	S	0.028± 0.011	0.628± 0.246	4.66	...	...	...	
1535+004	f	0.0	0.000	1.010	S	0.015± 0.008	0.364± 0.187	5.59	...	...	...	
1542+042	s	18.6	2.184	0.530	S	<0.012	< 0.257	4.47	...	...	...	
1546+027	s	18.5	0.415	1.270	S	0.076± 0.015	2.000± 0.387	6.72	...	...	...	
1548+056	s	18.5	1.422	1.830	S	<0.007	< 0.138	3.87	...	...	...	
1550−269	s	19.4	2.145	1.350	S	<0.008	< 0.239	11.03	...	...	...	
1555+001	f	22.1	1.770	2.010	S	<0.008	< 0.220	7.17	...	...	...	
1555−140	g	17.0	0.097	0.730	S	0.453± 0.034	14.400± 1.080	11.15	$1.74^{+0.31}_{-0.34}$	$8.45^{+42.62}_{-4.22}$	$1.48^{+3.10}_{-0.80}$	
(1557+032)	X	0.0	0.000	0.690	S	<0.006	< 0.146	6.02	...	...	...	
1556−245	s	17.8	2.818	0.690	S	<0.006	< 0.177	9.28	...	...	...	
1602−001	s	17.7	1.624	0.530	S	0.016± 0.008	0.444± 0.225	7.60	...	...	...	
1601−222	s	21.0	0.000	0.570	S	<0.013	< 0.408	11.03	...	...	...	
1614+051	s	21.1	3.217	0.670	S	0.023± 0.009	0.520± 0.212	4.90	...	...	...	
1615+029	s	18.2	1.339	0.740	S	<0.018	< 0.431	5.55	...	...	...	

Downloaded from https://academic.oup.com/mnras/article-abstract/301/1/261/1058213 by Library user on 07 September 2018

Table 1 – *continued*

Object (1)	Type (2)	m_B (3)	z (4)	$f_{2.7GHz}$ (5)	(6)	count s^{-1} (7)	F_x (8)	$N_{H,gal}$ (9)	Γ_{gal} (10)	$N_{H,free}$ (11)	Γ_{free} (12)	(13)
1616+063	s	19.6	2.086	0.930	S	<0.017	< 0.383	4.63	...	...	...	
1635−035	s	21.8	2.856	0.510	S	<0.008	< 0.259	10.79	...	...	...	
1648+015	f	22.7	0.000	0.720	S	<0.008	< 0.192	6.14	...	...	...	
1649−062	g	23.0	0.000	0.700	S	<0.005	< 0.127	11.17	...	...	...	
1654−020	f	0.0	0.000	0.640	S	<0.013	< 0.372	8.97	...	...	...	
1656+053	s	17.1	0.887	1.600	S	0.093± 0.016	2.290± 0.396	5.75	$0.88^{+0.54}_{-0.74}$	...	...	
1655+077	s	21.7	0.621	1.260	S	<0.013	< 0.328	6.55	...	...	...	
1705+018	s	18.5	2.576	0.530	S	<0.012	< 0.304	6.79	...	...	...	
1706+006	f	22.8	0.449	0.500	S	<0.017	< 0.464	7.86	...	...	...	
1725+044	s	18.2	0.296	0.780	SP	0.018± 0.009	0.502± 0.248	7.32	$2.01^{+0.64}_{-1.05}$	...	...	*
1732+094	f	0.0	0.000	1.080	S	<0.005	< 0.131	8.24	...	...	...	
1933−400	s	17.7	0.965	1.200	S	0.030± 0.014	0.885± 0.402	9.38	$3.16^{+0.86}_{-1.36}$	$4.79^{+45.86}_{-4.67}$	$2.22^{+3.64}_{-2.20}$	
1953−325	s	19.9	1.242	0.510	S	<0.027	< 0.762	8.16	...	...	...	
1954−388	s	17.8	0.626	2.000	S	0.025± 0.012	0.652± 0.322	6.51	...	...	...	
1958−179	s	17.0	0.650	1.110	S	0.094± 0.018	2.630± 0.511	7.85	...	...	...	
2000−330	s	19.6	3.783	0.710	UP	0.016± 0.002	0.346± 0.049	7.49	$1.56^{+0.27}_{-0.33}$	...	...	
2002−185	s	17.4	0.859	0.640	S	0.026± 0.010	0.686± 0.277	7.13	...	...	...	
2004−447	s	18.1	0.240	0.810	S	0.022± 0.011	0.427± 0.218	3.54	...	...	...	
2008−159	s	15.9	1.178	0.740	S	0.084± 0.017	2.020± 0.404	5.38	...	...	...	
2021−330	s	17.6	1.465	0.790	S	<0.020	< 0.508	5.93	...	...	...	
2022−077	s	18.5	1.388	1.120	S	<0.016	< 0.350	4.24	...	...	...	
2037−253	s	17.8	1.574	0.930	S	<0.010	< 0.226	4.78	...	...	...	
2044−168	s	17.5	1.937	0.770	S	<0.012	< 0.252	4.36	...	...	...	
2047+098	f	0.0	0.000	0.710	S	<0.008	< 0.205	6.87	...	...	...	
(2047+039)	Q	18.5	0.000	0.570	S	<0.010	< 0.275	7.33	...	...	...	
2053−044	s	19.0	1.177	0.550	S	<0.011	< 0.252	5.02	...	...	...	
2056−369	f	0.0	0.000	0.510	S	<0.010	< 0.228	4.79	...	...	...	
2059+034	s	17.6	1.013	0.590	S	0.022± 0.008	0.578± 0.221	6.95	$0.24^{+1.41}_{-0.24}$	...	...	
2058−135	g	10.6	0.029	0.600	S	0.028± 0.011	0.553± 0.223	4.08	...	...	...	
2058−297	s	16.2	1.492	0.650	S	<0.021	< 0.558	7.33	...	...	...	
2106−413	s	19.5	1.055	2.110	S	0.033± 0.012	0.653± 0.241	3.52	$0.95^{+0.86}_{-0.95}$	$0.17^{+45.11}_{-0.04}$	$0.15^{+5.19}_{-0.15}$	
2121+053	s	18.3	1.941	1.620	S	0.015± 0.008	0.374± 0.201	5.85	...	...	...	
2120+099	s	20.2	0.932	0.650	S	0.019± 0.009	0.440± 0.211	5.19	$0.04^{+1.73}_{-0.04}$	...	...	
2126−158	s	16.6	3.266	1.170	SP	0.107± 0.019	2.000± 0.358	4.93	$1.54^{+0.36}_{-0.46}$	$14.34^{+36.11}_{-9.78}$	$3.32^{+2.53}_{-1.97}$	*
2127−096	f	0.0	0.780	0.510	S	0.027± 0.011	0.590± 0.243	4.34	...	...	...	
2128−123	s	16.0	0.500	1.900	S	0.218± 0.027	5.420± 0.669	4.59	$2.02^{+0.25}_{-0.30}$	$4.20^{+4.80}_{-3.66}$	$1.91^{+1.24}_{-1.25}$	*
2131−021	s	18.6	1.285	1.910	UP	0.018± 0.002	0.407± 0.045	4.24	...	...	...	*
2134+004	s	16.5	1.937	7.590	SP	0.061± 0.015	1.150± 0.275	4.48	$1.20^{+0.43}_{-0.63}$	$9.58^{+29.74}_{-8.90}$	$2.18^{+3.52}_{-2.18}$	*
2135−248	s	17.3	0.821	0.770	S	<0.020	< 0.396	3.38	...	...	...	
2140−048	s	17.1	0.344	0.770	S	0.164± 0.024	3.580± 0.530	3.33	$2.29^{+0.27}_{-0.28}$	$5.46^{+6.29}_{-4.63}$	$2.96^{+1.82}_{-1.65}$	
2143−156	s	17.2	0.698	1.110	S	0.028± 0.012	0.607± 0.253	4.22	...	...	...	
2144+092	s	18.7	1.113	0.950	S	<0.011	< 0.269	5.14	...	...	...	
2145+067	s	16.8	0.999	3.300	SP	0.090± 0.018	1.750± 0.360	4.86	$1.45^{+0.38}_{-0.54}$	$7.49^{+43.33}_{-6.69}$	$2.00^{+3.86}_{-1.80}$	*
2145−176	s	20.2	2.130	0.820	S	0.017± 0.008	0.364± 0.173	3.94	...	...	...	
2149+056	f	0.0	0.740	1.010	S	<0.018	< 0.413	4.90	...	...	...	
2149+069	s	18.6	1.364	0.890	S	<0.018	< 0.419	4.86	...	...	...	
2149−307	s	17.7	2.345	1.320	S	0.434± 0.038	6.250± 0.549	1.91	$1.66^{+0.12}_{-0.14}$	$3.93^{+2.73}_{-2.37}$	$2.33^{+0.84}_{-0.83}$	
2155−152	s	18.1	0.672	1.670	S	0.027± 0.013	0.559± 0.269	3.75	$1.90^{+0.49}_{-0.70}$	$5.63^{+44.53}_{-5.48}$	$2.42^{+3.55}_{-2.41}$	
2200−238	s	17.7	2.120	0.530	S	<0.016	< 0.269	2.46	...	...	...	
2203−188	s	18.5	0.619	5.250	UP	0.009± 0.001	0.162± 0.022	2.66	...	...	...	*
2206−237	g	17.6	0.086	1.330	S	<0.007	< 0.118	2.40	...	...	...	
2208−137	s	16.8	0.392	0.720	S	0.124± 0.024	2.930± 0.557	3.59	$2.35^{+0.32}_{-0.36}$	$0.22^{+4.89}_{-0.11}$	$1.09^{+1.79}_{-0.49}$	
2210−257	s	17.9	1.833	0.960	S	<0.024	< 0.336	1.81	...	...	...	
2212−299	s	17.2	2.703	0.540	S	<0.029	< 0.326	1.11	...	...	...	
2215+020	s	22.0	3.572	0.700	S	<0.021	< 0.470	4.76	...	...	...	
2216−038	s	16.6	0.901	1.040	S	0.045± 0.016	1.090± 0.399	5.60	$2.64^{+0.48}_{-0.61}$	$13.42^{+27.92}_{-10.86}$	$4.68^{+1.32}_{-3.09}$	
2223−052	s	17.1	1.404	4.700	SP	0.039± 0.016	0.828± 0.334	5.08	$1.86^{+0.59}_{-0.99}$	$6.59^{+25.57}_{-6.43}$	$2.22^{+3.76}_{-2.19}$	*
(2224+006)	X	0.0	0.000	0.520	S	<0.006	< 0.134	4.85	...	...	...	
2227−088	s	18.0	1.561	1.490	S	<0.014	< 0.314	4.51	...	...	...	
2227−399	s	17.4	0.323	1.020	SP	0.509± 0.043	5.750± 0.481	1.20	$1.98^{+0.11}_{-0.12}$	$2.01^{+2.58}_{-1.91}$	$2.31^{+0.96}_{-0.92}$	*

Downloaded from https://academic.oup.com/mnras/article-abstract/301/1/261/1058213 by Library user on 07 September 2018

Table 1 – *continued*

Object (1)	Type (2)	m_B (3)	z (4)	$f_{2.7GHz}$ (5)	(6)	count s^{-1} (7)	F_x (8)	$N_{H,gal}$ (9)	Γ_{gal} (10)	$N_{H,free}$ (11)	Γ_{free} (12)	(13)
2229−172	f	21.3	1.780	0.520	S	<0.014	< 0.272	3.26	...	...	...	
2233−148	s	20.9	0.609	0.500	S	0.039± 0.016	0.866± 0.354	4.46	...	...	...	
2239+096	s	19.7	1.707	0.650	S	0.028± 0.010	0.699± 0.260	5.89	$2.87^{+0.71}_{-1.00}$	$11.73^{+21.40}_{-11.56}$	$4.43^{+1.56}_{-4.21}$	
2240−260	s	17.9	0.774	1.080	SP	0.059± 0.023	0.739± 0.292	1.46	...	...	...	*
2243−123	s	16.5	0.630	2.740	S	0.111± 0.031	2.540± 0.717	4.78	$2.92^{+0.50}_{-0.56}$	$9.18^{+11.29}_{-9.04}$	$4.31^{+1.66}_{-3.72}$	
2245+029	s	19.5	0.000	0.660	UP	0.022± 0.003	0.532± 0.066	5.22	$2.55^{+0.35}_{-0.38}$	$10.24^{+29.66}_{-5.83}$	$3.36^{+2.38}_{-1.14}$	
2245−328	s	18.2	2.268	2.010	S	<0.020	< 0.238	1.23	...	...	...	
2252−090	s	0.0	0.606	0.630	S	<0.022	< 0.439	3.65	...	...	...	
2254−367	g	11.4	0.006	0.820	SP	0.084± 0.023	0.992± 0.271	1.15	$1.01^{+0.36}_{-0.47}$	$4.18^{+18.85}_{-4.05}$	$1.96^{+2.19}_{-1.87}$	
2255−282	s	16.6	0.925	1.380	S	0.040± 0.020	0.636± 0.324	2.35	...	...	...	
2300−189	s	18.5	0.129	0.980	S	0.424± 0.056	7.250± 0.958	2.42	$2.19^{+0.18}_{-0.19}$	$3.45^{+4.41}_{-3.27}$	$2.55^{+1.43}_{-1.35}$	
2301+060	s	17.7	1.268	0.520	S	<0.013	< 0.326	5.63	...	...	...	
2303−052	s	18.3	1.136	0.540	S	0.026± 0.012	0.562± 0.247	4.09	...	...	...	
2304−230	f	0.0	0.000	0.590	S	<0.029	< 0.436	2.13	...	...	...	
2312−319	s	17.6	1.323	0.710	S	<0.083	< 1.050	1.47	...	...	...	
(2311−452)	Q	19.0	0.000	1.910	S	<0.015	< 0.217	1.82	...	...	...	
(2314−340)	Q	18.5	0.000	0.620	S	<0.026	< 0.370	1.88	...	...	...	
2314−409	s	18.2	2.448	0.500	S	<0.014	< 0.191	1.73	...	...	...	
2313−438	s	19.0	1.847	0.860	S	<0.015	< 0.237	2.21	...	...	...	
2318+049	s	18.6	0.622	1.230	S	0.041± 0.012	2.340± 0.684	5.66	$3.05^{+0.46}_{-0.53}$	$6.17^{+11.30}_{-6.05}$	$3.18^{+2.80}_{-2.44}$	
2320+079	s	17.6	2.090	0.700	S	<0.007	< 0.158	5.11	...	...	...	
(2320−035)	Q	18.6	1.410	0.890	S	<0.011	< 0.229	4.00	...	...	...	
2325−150	s	19.5	2.465	0.630	S	<0.013	< 0.193	2.06	...	...	...	
2329−162	s	20.9	1.155	0.980	S	0.019± 0.010	0.269± 0.138	1.79	...	...	...	
2329−384	s	17.1	1.202	0.770	S	<0.033	< 0.413	1.43	...	...	...	
2330+083	f	0.0	0.000	0.520	S	<0.007	< 0.159	5.31	...	...	...	
2329−415	s	18.2	0.671	0.510	S	<0.054	< 0.786	1.92	...	...	...	
2331−240	g	16.5	0.048	1.040	S	0.399± 0.038	5.510± 0.524	1.73	$1.82^{+0.14}_{-0.13}$	$3.91^{+2.87}_{-2.44}$	$2.59^{+0.92}_{-0.89}$	
2332−017	s	18.4	1.184	0.640	S	<0.026	< 0.529	3.72	...	...	...	
2335−027	s	18.1	1.072	0.600	S	<0.018	< 0.382	4.08	...	...	...	
2335−181	s	16.8	1.450	0.690	S	0.041± 0.014	0.600± 0.208	1.95	$2.07^{+0.55}_{-0.56}$	...	...	
2337−334	f	0.0	0.000	1.360	S	<0.030	< 0.338	1.11	...	...	...	
2344+092	s	16.1	0.673	1.600	SP	0.084± 0.016	2.470± 0.458	5.25	$2.21^{+0.33}_{-0.39}$	$10.85^{+36.04}_{-6.71}$	$3.56^{+2.40}_{-1.74}$	*
2344−192	f	0.0	0.000	0.540	S	<0.009	< 0.131	1.91	...	...	...	
2345−167	s	17.3	0.576	4.080	S	0.057± 0.016	0.851± 0.234	2.05	...	...	...	
2351−006	s	18.0	0.464	0.510	S	<0.010	< 0.197	3.41	...	...	...	
2351−154	s	18.6	2.675	1.080	SP	0.038± 0.013	0.579± 0.192	2.18	$1.36^{+0.47}_{-0.68}$	$2.95^{+39.41}_{-2.82}$	$1.60^{+4.12}_{-1.55}$	*
2354−117	s	17.8	0.960	1.570	S	0.032± 0.013	0.548± 0.218	2.69	$1.57^{+0.55}_{-0.86}$	...	...	
2358−161	s	18.3	2.033	0.500	S	<0.013	< 0.209	2.24	...	...	...	

Column (1) Object name. Objects in brackets do not belong to the complete sample. Column (2) Identification from plate according to Drinkwater et al. (1997) and Peterson (private communication). 's' = stellar, 'g' = galaxy, 'f' = faint, 'X' = crowded field, 'D' = double galaxy, 'B' = BL Lac candidate, 'Q' = quasar, 'E' = elliptical galaxy. Column (3) Blue magnitude (B_J) according to Drinkwater et al. (1997). Column (4) Redshift. Column (5) Radio flux density at 2.7 GHz in Jy. Column (6) Reference to the X-ray detection. 'S' = Survey, 'P' = pointed observation. Column (7) X-ray count rate in the *ROSAT* energy band (0.1–2.4 keV). In general the Survey count rate is given, except for the sources that are detected in pointed observations only. Upper limits are 90 per cent confidence. Column (8) Total 0.1–2.4 keV X-ray flux in units of 10^{-12} erg cm^{-2} s^{-1}. The calculation was done assuming Galactic absorption only and the average X-ray photon index for radio-loud quasars ($\Gamma = 2.0$). The individual photon index for a source was used in the calculation whenever it was available and well determined (i.e. $\Delta\Gamma < 0.5$). Column (9) Galactic N_H value in 10^{20} cm^{-2} (Dickey & Lockman 1990). Column (10) X-ray photon index Γ_{gal}. Errors are 1σ. For sources detected in pointed observations, it was determined by an explicit fit of a power-law model to the data. For sources detected in the RASS only it was computed using a hardness ratio technique (Schartel 1996). In both cases the Galactic N_H value was assumed. Columns (11) and (12) Results of the two-parameter spectral fits. The fitted absorption ($N_{H,free}$) and the respective power-law index (Γ_{free}) are given. Column (13) An asterisk denotes the sources that have spectral parameters available also from explicit fits to the data. The results of the fits are presented in Table 2.

3.3 Spectral analysis

In general, simple power-law models for the X-ray spectra modified by neutral gas absorption were considered in the analysis. The amount of absorption is parametrized by the column density of neutral hydrogen in the line of sight to the source (the N_H value), assuming standard element abundances and the energy-dependent absorption cross-sections of Morrison & McCammon (1983). The Galactic N_H values were determined from radio measurements (Dickey & Lockman 1990). For each source two photon indices were determined, one by fixing the absorption to the Galactic value, the other one by leaving the amount of absorption as a free parameter.

For weak sources (mostly from the RASS) a technique based on hardness ratios was applied to estimate the spectral parameters. The two standard *ROSAT* hardness ratios are defined as $HR_1 = (B - A)/(B + A)$ and $HR_2 = (D - C)/(D + C)$, where A, B, C and D are the number of photons in the pulse height channel intervals

Downloaded from https://academic.oup.com/mnras/article-abstract/301/1/261/1058213 by Library user on 07 September 2018

Table 2. Results from spectral fitting.

Name (1)	Γ_{gal} (2)	χ^2_{red} (3)	Γ_{free} (4)	$N_{H,free}$ (5)	χ^2_{red} (6)
0048−097	$2.57^{+0.07}_{-0.07}$	0.82(92)	$2.79^{+0.24}_{-0.24}$	$4.20^{+0.72}_{-0.68}$	0.77(91)
0118−272	$2.39^{+0.14}_{-0.14}$	0.93(15)	$2.84^{+0.56}_{-0.50}$	$2.79^{+1.56}_{-1.25}$	0.81(14)
0122−003	$2.16^{+0.12}_{-0.13}$	0.92(24)	$1.72^{+0.30}_{-0.28}$	$1.96^{+0.86}_{-0.67}$	0.67(23)
0135−247	$2.18^{+0.09}_{-0.08}$	1.20(28)	$1.82^{+0.22}_{-0.20}$	$0.59^{+0.42}_{-0.35}$	0.94(27)
0137+012	$1.94^{+0.06}_{-0.05}$	1.08(20)	$1.99^{+0.16}_{-0.16}$	$3.21^{+0.52}_{-0.49}$	1.12(19)
0232−042	$2.27^{+0.07}_{-0.07}$	1.15(32)	$1.96^{+0.20}_{-0.19}$	$1.74^{+0.52}_{-0.47}$	0.96(31)
0238−084	$1.53^{+0.15}_{-0.17}$	0.88(15)	$1.58^{+0.36}_{-0.37}$	$3.30^{+1.62}_{-1.35}$	0.98(14)
0301−243	$2.83^{+0.11}_{-0.10}$	0.91(23)	$2.77^{+0.31}_{-0.27}$	$1.62^{+0.62}_{-0.53}$	0.95(22)
0316−444	$1.86^{+0.02}_{-0.02}$	1.99(80)	$1.56^{+0.07}_{-0.07}$	$1.56^{+0.20}_{-0.20}$	1.14(79)
0403−132	$1.71^{+0.09}_{-0.09}$	0.95(22)	$1.75^{+0.23}_{-0.23}$	$3.80^{+0.90}_{-0.90}$	0.99(21)
0405−123	$2.36^{+0.05}_{-0.06}$	0.91(19)	$2.23^{+0.17}_{-0.16}$	$3.46^{+0.53}_{-0.50}$	0.87(18)
0426−380	$1.95^{+0.27}_{-0.27}$	2.93(6)	$3.20^{+1.35}_{-1.16}$	$5.28^{+3.82}_{-3.02}$	2.36(5)
0430+052	$1.85^{+0.06}_{-0.06}$	1.85(51)	$2.52^{+0.30}_{-0.24}$	$19.66^{+4.68}_{-3.50}$	0.95(50)
0438−436	$0.70^{+0.10}_{-0.10}$	2.32(19)	$1.96^{+1.48}_{-0.51}$	$11.00^{+26.43}_{-5.35}$	0.62(18)
0500+019	$0.71^{+0.56}_{-0.63}$	0.93(8)	$2.22^{+2.91}_{-2.04}$	$39.52^{+60.47}_{-35.46}$	0.91(7)
0537−441	$2.54^{+0.13}_{-0.13}$	1.56(35)	$2.04^{+0.32}_{-0.32}$	$2.54^{+0.99}_{-0.85}$	1.30(34)
0537−286	$1.32^{+0.14}_{-0.16}$	1.11(15)	$1.59^{+0.36}_{-0.35}$	$3.11^{+1.48}_{-1.23}$	1.06(14)
1034−293	$2.01^{+0.22}_{-0.26}$	1.76(16)	$1.27^{+0.39}_{-0.38}$	$1.27^{+1.17}_{-0.93}$	1.08(15)
1055+018	$2.37^{+0.18}_{-0.19}$	1.42(11)	$1.64^{+0.47}_{-0.43}$	$1.62^{+1.36}_{-1.08}$	0.85(10)
1136−135	$2.36^{+0.50}_{-0.50}$	1.00(10)	$2.24^{+1.58}_{-1.58}$	$3.20^{+5.70}_{-3.20}$	1.11(9)
1145−071	$1.80^{+0.55}_{-0.82}$	0.28(4)	$1.52^{+1.06}_{-1.08}$	$2.30^{+8.99}_{-2.30}$	0.30(3)
1144−379	$2.54^{+0.17}_{-0.19}$	0.81(34)	$2.67^{+0.39}_{-0.37}$	$9.48^{+2.50}_{-1.88}$	0.81(33)
1226+023	$2.30^{+0.01}_{-0.02}$	1.31(56)	$2.16^{+0.05}_{-0.06}$	$1.45^{+0.13}_{-0.12}$	1.01(55)
1253−055	$1.90^{+0.07}_{-0.06}$	0.60(21)	$1.89^{+0.20}_{-0.19}$	$2.23^{+0.62}_{-0.57}$	0.63(20)
1302−102	$2.36^{+0.09}_{-0.09}$	0.71(29)	$2.12^{+0.26}_{-0.24}$	$2.63^{+0.77}_{-0.70}$	0.65(28)
1330+022	$1.82^{+0.06}_{-0.06}$	1.05(14)	$1.86^{+0.20}_{-0.19}$	$1.87^{+0.52}_{-0.47}$	1.12(13)
1334−127	$1.73^{+0.15}_{-0.16}$	1.21(14)	$2.09^{+0.18}_{-0.36}$	$6.77^{+2.42}_{-1.79}$	1.05(13)
1351−018	$1.86^{+0.30}_{-0.37}$	1.67(12)	$1.14^{+0.51}_{-0.46}$	$0.82^{+1.54}_{-0.82}$	1.20(11)
1510−089	$1.92^{+0.15}_{-0.15}$	0.99(29)	$1.77^{+0.29}_{-0.29}$	$6.80^{+0.70}_{-0.70}$	0.97(28)
1519−273	$2.03^{+0.38}_{-0.43}$	1.16(9)	$2.37^{+2.63}_{-0.93}$	$11.84^{+37.32}_{-6.09}$	1.22(8)
1725+044	$2.01^{+0.23}_{-0.25}$	0.79(11)	$2.63^{+1.82}_{-0.90}$	$12.83^{+14.01}_{-6.60}$	0.72(10)
2126−158	$1.06^{+0.15}_{-0.17}$	1.04(22)	$1.52^{+0.55}_{-0.35}$	$8.81^{+8.69}_{-2.79}$	0.77(21)
2128−123	$2.16^{+0.42}_{-0.42}$	0.52(8)	$2.36^{+1.16}_{-1.16}$	$5.60^{+4.45}_{-4.90}$	0.57(7)
2131−021	$2.05^{+0.41}_{-0.47}$	0.41(4)	$1.86^{+1.27}_{-1.18}$	$3.51^{+5.12}_{-3.24}$	0.50(3)
2134+004	$1.44^{+0.18}_{-0.19}$	1.08(14)	$1.72^{+0.39}_{-0.39}$	$6.06^{+2.75}_{-1.89}$	1.03(13)
2145+067	$1.47^{+0.26}_{-0.31}$	0.48(11)	$1.69^{+0.59}_{-0.54}$	$6.28^{+5.52}_{-2.71}$	0.46(10)
2203−188	$2.28^{+0.41}_{-0.41}$	0.70(12)	$3.00^{+1.25}_{-1.25}$	$5.30^{+5.70}_{-5.30}$	0.69(11)
2223−052	$1.73^{+0.10}_{-0.11}$	1.29(39)	$2.03^{+0.24}_{-0.22}$	$6.73^{+1.28}_{-1.10}$	1.15(38)
2227−399	$2.15^{+0.05}_{-0.05}$	0.94(51)	$2.10^{+0.17}_{-0.16}$	$1.08^{+0.38}_{-0.33}$	0.95(50)
2240−260	$2.15^{+0.33}_{-0.29}$	0.84(5)	$1.79^{+0.42}_{-0.69}$	$0.78^{+2.22}_{-0.78}$	0.87(4)
2344+092	$2.31^{+0.12}_{-0.14}$	0.76(29)	$2.00^{+0.29}_{-0.28}$	$3.99^{+1.07}_{-0.99}$	0.66(28)
2351−154	$1.32^{+0.14}_{-0.15}$	1.65(13)	$1.89^{+0.43}_{-0.42}$	$4.45^{+1.95}_{-1.61}$	1.31(12)

11–41, 52–201, 52–90 and 91–201, respectively. Every combination of photon index Γ and absorption N_H leads to unique values for the two hardness ratios when folded with the instrument response. The inversion of this procedure then allows us to determine the spectral parameters from the measured hardness ratios. However, this method only gives a rough estimate of the spectral parameters, in particular for the two-parameter fits. A detailed discussion of the method is presented in Schartel (1996). In total we obtained spectral information for 104 sources in this way.

Whenever a pointed PSPC observation was available for a source from the public archive and if a sufficient number of source photons ($\gtrsim 50$) were accumulated in this pointing, we determined the spectral parameters by explicitly fitting a power-law model to the data. X-ray spectra of 42 sources were determined in this way with increased accuracy. The results are presented in Table 2. A few sources were observed more than once with the PSPC (e.g. 3C 279). In these cases the observation with the longest exposure was chosen for the spectral analysis. If the number of photons was too low for

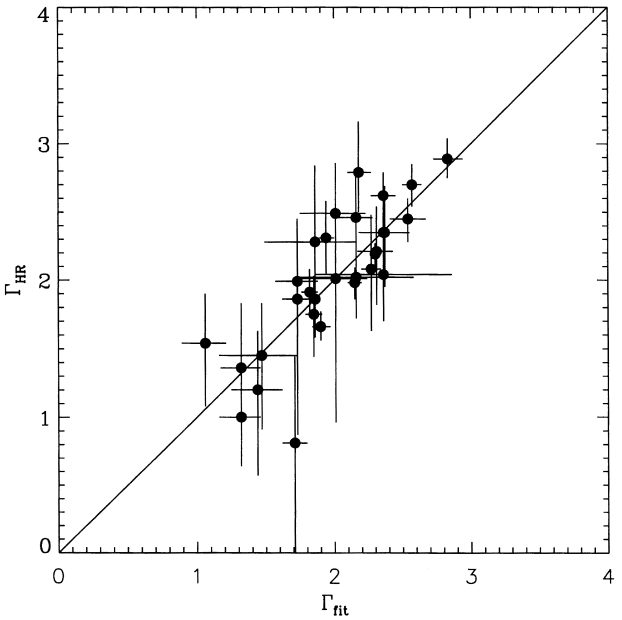

Figure 1. Comparison of the photon indices derived from the hardness ratios with those from spectral fits to pointed observations for the 30 objects, where both RASS and pointed data were available. Only the fits for fixed Galactic N_H are shown.

spectral fitting, we again used the hardness ratios (this time derived from the *pointed* observation) to determine the spectral parameters.

In total, spectral information could be obtained for 115 sources of the sample. The X-ray spectra are discussed in Section 4.4.

For 30 sources we have spectral information from both the RASS and pointed observations. In order to validate the hardness ratio method, we compare in Fig. 1 the photon indices derived from the hardness ratios with those determined from spectral fits. In general, the two independently derived photon indices agree very well. For all sources the results agree within their respective 2 σ errors.

3.4 The tables

The X-ray properties of the Parkes sample of flat-spectrum radio sources are summarized in Table 1. For a detailed description of its contents we refer to the table notes. In columns (10) to (12) we give the spectral parameters as derived from the hardness ratios only, either from the RASS or (in some cases) from pointed observations. In column (13) we indicate if a detailed fit is available. The parameters derived from spectral fitting are given in Table 2.

4 RESULTS

4.1 X-ray detection rates

163 sources (∼51 per cent) of the complete sample were detected in soft X-rays at the 3σ confidence level. For the remaining 160 objects the 2σ upper limits to the X-ray count rates were determined. If only the RASS data are considered the number of detections is reduced to 151 (∼47 per cent).

In this section we will discuss how the probability of a source to be detected in X-rays depends on various source parameters. Only the results from the RASS are used in this analysis in order to avoid any bias by the usually much longer observation times of the pointed *ROSAT* observations.

To begin with, we note that the distributions of detections and

Downloaded from https://academic.oup.com/mnras/article-abstract/301/1/261/1058213 by Library user on 07 September 2018

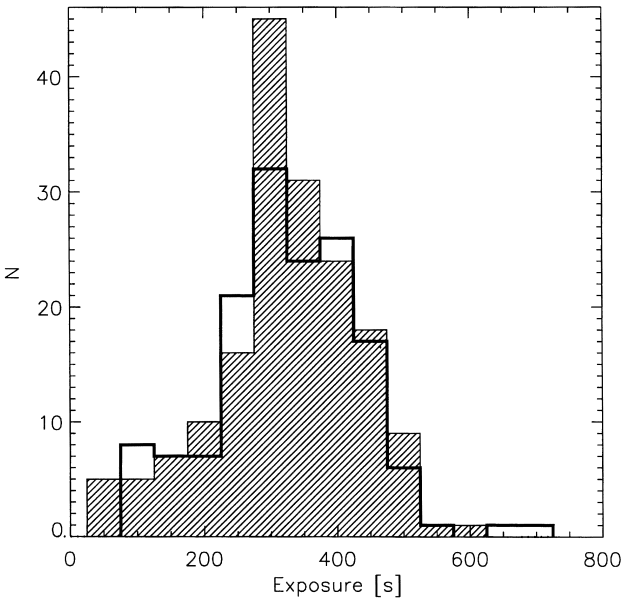

Figure 2. Distribution of the effective RASS exposures for the sources detected (solid line) and the sources with upper limits (hatched). The two distributions are indistinguishable.

upper limits are not significantly different in terms of the RASS exposure. This is illustrated in Fig. 2. The RASS exposures range from 65 s to about 730 s with a median of 348 s. A Kolmogorov–Smirnov (KS) test gives a probability of $P = 0.996$, i.e. the two distributions are practically identical.

However, as shown in Fig. 3, the distribution of upper limits (hatched) is systematically shifted towards higher Galactic $N_{\rm H}$ values. A KS test gives $P = 0.048$, i.e. the hypothesis that the two distributions are the same can be rejected at a significance level of 4.8 per cent. A high value for the Galactic absorption certainly reduces the probability for a source to be detected in soft X-rays, but

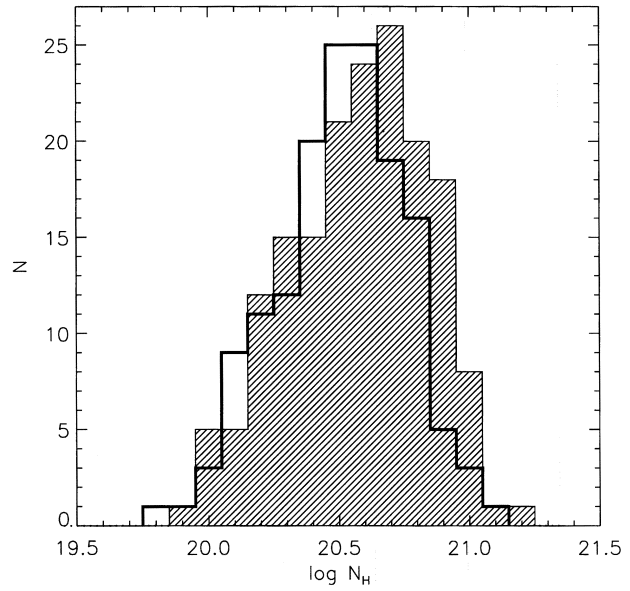

Figure 3. Histogram of the Galactic $N_{\rm H}$ values for the sources detected in the RASS (solid line) and the sources with upper limits (hatched). Note the shift towards higher $N_{\rm H}$ values for upper limit sources.

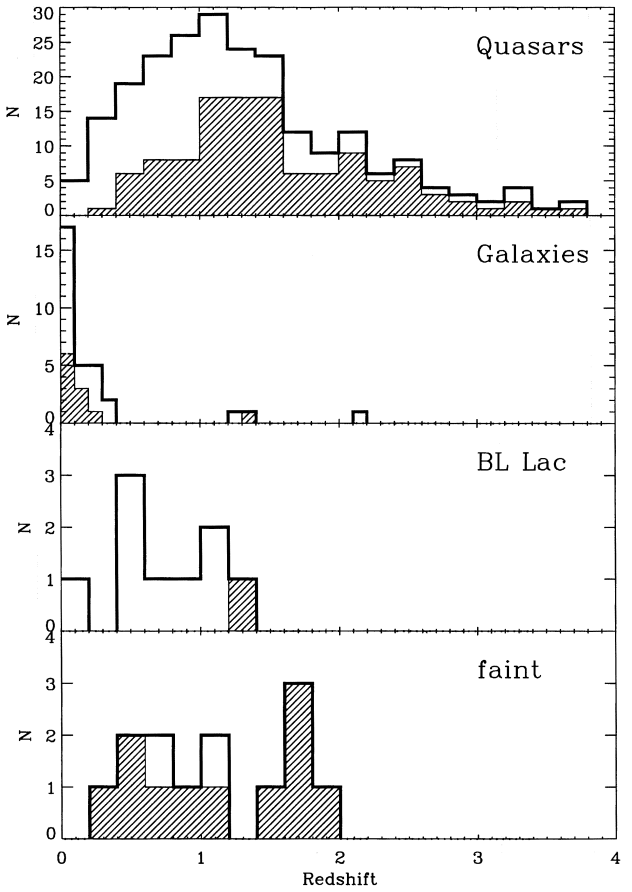

Figure 4. Redshift distributions for the main classes of objects in the sample. The distribution for the *total* number of objects in each class (i.e. detections plus upper limits) is drawn with a solid line, whereas the upper limit sources are represented by the hatched areas.

the influence is difficult to quantify. In any case, this effect is hardly the main reason for a source not to be detected in the RASS.

The detection rates for the various optical classifications are ~47.0 per cent (110 out of 234) for quasars, 62.9 per cent (22 out of 35) for galaxies and 15.8 per cent (6 out of 38) for 'faint' sources. 13 out of the 14 BL Lac objects in the sample are detected in the RASS. The only exception is PKS 2131–021, a bona fide BL Lac from the 1-Jy sample. It is only detected in a ~8-ks pointed observation. Both currently unidentified objects are not seen in the RASS.

Fig. 4 shows the redshift distributions of the various object classes. In each panel the distribution of the total number of objects, i.e. detections plus upper limits, in the respective class is plotted as a solid line. The upper limits alone are represented by the hatched area.

226 quasars have known redshifts and the average redshift is $z = 1.32$. Obviously, the fraction of upper limits increases with redshift. The average redshift of the detected quasars is $z = 1.08$, compared with $z = 1.55$ for the non-detections. A KS test confirms that the two distributions are different ($P \approx 1.2 \times 10^{-6}$). Not surprisingly, this suggests that the distance of the source is the main parameter influencing the X-ray detection probability. A similar trend holds for BL Lac objects, although the involved number is small. PKS 2131–021, the only non-detected BL Lac object, happens to be at the highest redshift ($z = 1.285$). Note that the redshift reported by Drinkwater et al. (1997) is different from the (unconfirmed) value published previously ($z = 0.557$: Wills & Lynds 1978; Stickel et al.

Downloaded from https://academic.oup.com/mnras/article-abstract/301/1/261/1058213 by Library user on 07 September 2018

Table 3. Average and median of the redshift distributions of the various object classes.

Class (1)	N (2)	Total (3)	Detections (4)	Upper limits (5)
Quasars	226	1.32 (1.18)	1.06 (0.91)	1.56 (1.42)
Galaxies	32	0.25 (0.10)	0.27 (0.10)	0.21 (0.09)
BL Lacs	9	0.74 (0.77)	0.67 (0.77)	1.29 (...)
'faint'	13	1.11 (1.02)	0.98 (1.18)	1.13 (1.02)

Columns. (1) Object class. (2) Number of objects with known redshift. (3) Average redshift of the total number of objects in the respective class. The value in brackets gives the median. (4) and (5) The same for detections and upper limits.

1991). No trend with redshift is visible for the galaxies and the optically 'faint' objects. Comparing the redshift distributions of the detected and the undetected objects, the KS test gives $P = 0.89$ and 0.88 for galaxies and 'faint' objects, respectively. This indicates that properties intrinsic to the sources also influence the detection probability, like for example the optical or the radio luminosity. The statistical properties of the redshift distributions of all object classes are summarized in Table 3.

The 44 sources without known redshifts do not affect our conclusion that distance is the main factor that determines the probability for X-ray detection. Only eight out 234 quasars (~3 per cent) have no redshift. Although 25 of the 38 'faint' sources have no redshift, the comparison of the detection rates for sources with and without redshift shows that these are identical.

4.2 X-ray positions

We compared the X-ray positions derived from the RASS data with the radio positions of the sample sources. Angular distances up to ~75 arcsec were found, although the majority of the X-ray sources lie within 50 arcsec of the radio position, which corresponds to about 2.5σ of the average positional accuracy in the RASS (Voges 1992). The positional differences are mainly due to the X-ray observation, because the optical/radio positions from the flat-spectrum Parkes sample are known with arcsecond accuracy (Drinkwater et al. 1997). We are therefore confident that the X-ray sources detected are truly associated with the radio sources. There is one X-ray source at a distance of 164 arcsec from the radio position of 1509+022. This X-ray source is also included in the *ROSAT* Bright Source catalogue (Voges et al. 1998), which is based on the latest reprocessing of the Survey data (RASS II). The position derived from these data corresponds to within 8 arcsec to the radio source position. We therefore keep 1509+022 as an X-ray detection, because the large positional difference is obviously due to an inaccurate attitude solution of the RASS I data.

4.3 Variability

37 sources were detected in the RASS and in one or more *ROSAT* PSPC pointings. We are therefore able to compare the X-ray count rates from these observations. Variability is parametrized by the ratio of the maximum and the minimum observed count rates. The distribution of this quantity is shown in Fig. 5. For about 40 per cent of the sources the observed variations are below 40 per cent and can thus not be distinguished from statistical fluctuations. Only four sources (~11 per cent) have varied by more than a factor of 3 (the quasars 3C 279 and PKS 1510−089, as well as the BL Lac objects

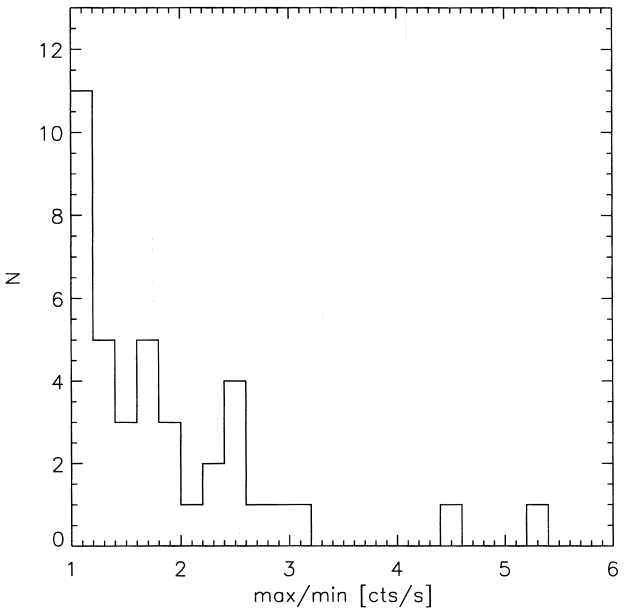

Figure 5. The ratio of the maximum and the minimum measured count rates for objects detected in both the RASS and pointed PSPC observations. For clarity, the most variable object (PKS 1514−241) is not shown in the diagram. It varied by more than a factor of 17 within the two observations (see text).

PKS 1514−241 and PKS 1519−273). As already noted by Siebert et al. (1996), the most extreme object is the BL Lac PKS 1514−241 (Ap Lib), which is clearly detected in the RASS, but not in a 2.8-ks pointed PSPC observation. The upper limit from the latter observation implies that Ap Lib varied by more than a factor of 17 within 3 yr.

The distribution in Fig. 5 looks very similar to the corresponding distribution for the bulk of radio-loud quasars, as for example described in Brinkmann et al. (1997a, see their fig. 2). Therefore, within the limits of small-number statistics, the flat-spectrum Parkes radio sources do not seem to exhibit larger X-ray variability than 'ordinary' radio-loud quasars.

4.4 X-ray spectra

As described in Section 3.3, we determined the spectral parameters for an absorbed power-law model for more than 100 sources of the sample either by explicitly fitting the model to the data or by applying the hardness ratio technique. In particular, the latter method usually results in rather large uncertainties on the individual parameters, and we therefore take a statistical approach to investigate the spectral properties of flat-spectrum radio sources.

We investigated the resulting photon index distributions for quasars, BL Lac objects and galaxies using a maximum-likelihood procedure (Maccacaro et al. 1988), which gives an estimate of the mean and the *intrinsic* dispersion of a supposed parent distribution and which takes into account the errors on the individual data points. The results of this analysis are presented in Fig. 6 and in Table 4.

The average photon index for the flat-spectrum quasars is $\langle\Gamma\rangle \approx 1.95^{+0.13}_{-0.12}$ for fixed Galactic $N_{\rm H}$, and it remains the same when absorption is considered as a free parameter. The soft X-ray spectra of flat-spectrum radio-loud quasars are thus flatter ($\Delta\Gamma\sim$ 0.25) than those of 'ordinary' radio-loud quasars ($\langle\Gamma\rangle \sim 2.2$: cf. Brunner et al. 1992; Brinkmann et al. 1995) with a similar redshift

Downloaded from https://academic.oup.com/mnras/article-abstract/301/1/261/1058213 by Library user on 07 September 2018

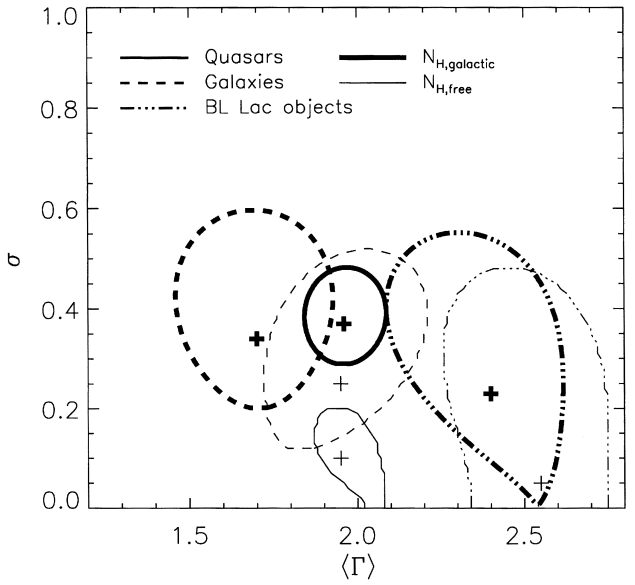

Figure 6. Result of the maximum-likelihood analysis of the distribution of X-ray spectral indices for quasars, galaxies and BL Lac objects (mean $\langle\Gamma\rangle$ and intrinsic dispersion σ) for both fixed Galactic $N_{\rm H}$ (thick lines) and free $N_{\rm H}$ (thin lines). The crosses correspond to the best-fitting parameters, whereas the contours represent the 90 per cent confidence ranges.

range. The latter point is important because of the well-known redshift dependence of the soft X-ray photon index (Schartel et al. 1996; Brinkmann et al. 1997a), which will be discussed below.

If we only consider sources with $z < 1$ in the maximum-likelihood analysis, the average spectral index for fixed $N_{\rm H}$ steepens to $\langle\Gamma\rangle \sim 2.1 \pm 0.1$. This result is completely consistent with the results of Brinkmann et al. (1997a) for an inhomogeneous sample of flat-spectrum quasars with $z < 1$ from the Véron–Véron catalogue. We thus confirm that the X-ray spectrum of flat-spectrum quasars is on average flatter than that of steep-spectrum quasars by $\Delta\Gamma \sim 0.1-0.2$.

The non-zero dispersion σ of the photon index distribution for quasars indicates that not only is the width of the distribution due to statistical fluctuations, but also the distribution is intrinsically broadened. This is not surprising, since the measured photon index also depends on several other source parameters, like for example redshift (see Fig. 7) and radio spectral index (see Fig. 8). The intrinsic dispersion of the distribution is significantly smaller for the fits with $N_{\rm H,free}$. This might indicate either that a simple absorbed power-law is not a valid description of the soft X-ray spectrum for a number of sources, or that the spectra are altered by

Table 4. Best-fitting parameters for the photon index distributions from a maximum-likelihood analysis.

		Galactic $N_{\rm H}$			free $N_{\rm H}$	
Class	N	Γ	σ	N	Γ	σ
(1)	(2)	(3)	(4)	(5)	(6)	(7)
quasars	83	$1.95^{+0.13}_{-0.12}$	$0.37^{+0.11}_{-0.08}$	69	$1.95^{+0.13}_{-0.08}$	$0.10^{+0.10}_{-0.10}$
BL Lacs	10	$2.40^{+0.12}_{-0.31}$	$0.23^{+0.32}_{-0.22}$	10	$2.55^{+0.20}_{-0.29}$	$0.05^{+0.43}_{-0.05}$
galaxies	17	$1.70^{+0.23}_{-0.24}$	$0.34^{+0.26}_{-0.14}$	15	$1.95^{+0.26}_{-0.23}$	$0.25^{+0.27}_{-0.13}$

Columns. (1) Object class. (2) Number of objects used in the analysis with fixed Galactic $N_{\rm H}$. (3) and (4) Best-fitting mean Γ and width σ for the underlying parent population. Errors are 90 per cent confidence. (5)–(7) The same as (1)–(3), but for the distributions resulting from the analysis with $N_{\rm H}$ as a free parameter.

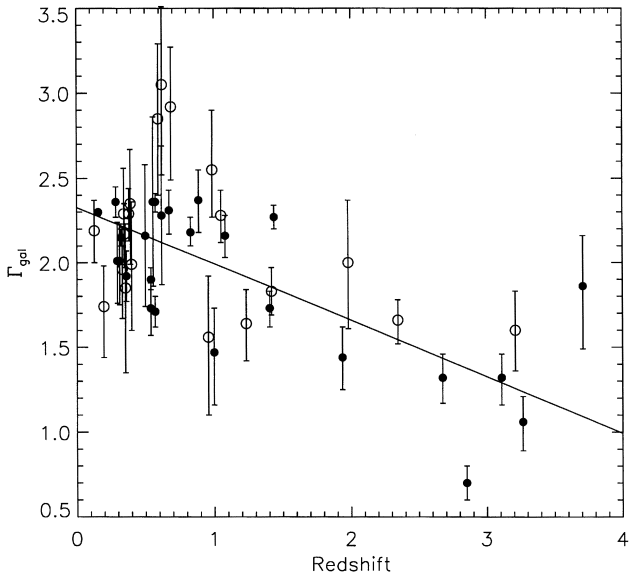

Figure 7. The photon index Γ (for fixed Galactic $N_{\rm H}$) as a function of redshift for sources with errors $\Delta\Gamma < 0.5$. The straight line indicates the best-fitting regression result. Open circles represent sources with the photon index derived from hardness ratios, whereas filled circles denote objects with fits to data from pointed observations.

additional absorption. The latter idea will be discussed in detail in Section 5. Here we only note that the quasar with the flattest X-ray spectrum for fixed Galactic $N_{\rm H}$ is PKS 0438–436 at $z = 2.85$ ($\Gamma \approx 0.7 \pm 0.1$). The fit, however, is statistically not acceptable (cf. Table 2). The free absorption result indicates additional absorption in the line of sight, which seems to be quite common for high-redshift radio-loud quasars (Elvis et al. 1994; Cappi et al. 1997).

The BL Lac objects contained in the sample have significantly steeper soft X-ray spectra than the other object classes ($\langle\Gamma\rangle \approx 2.4$).

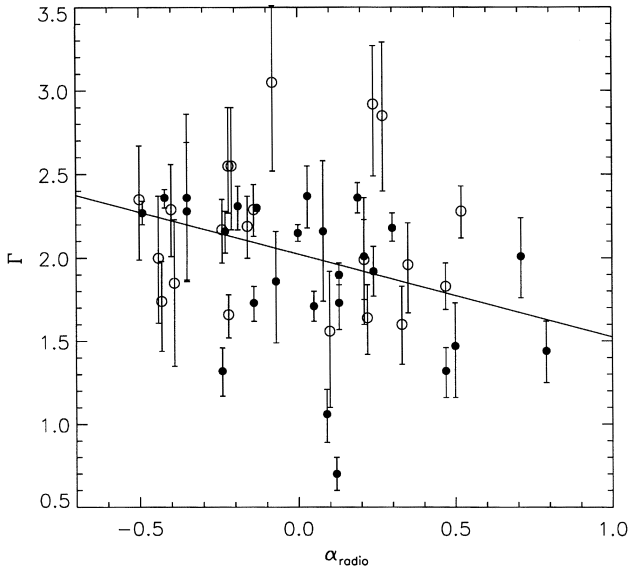

Figure 8. The photon index Γ at fixed $N_{\rm H}$ as a function of the radio spectral index α between 2.7 GHz and 5 GHz for sources with well-determined photon indices ($\Delta\Gamma < 0.5$). The straight line indicates the best-fitting regression result. Open circles represent sources with the photon index derived from the hardness ratios, whereas filled circles denote objects with fits to the data.

Downloaded from https://academic.oup.com/mnras/article-abstract/301/1/261/1058213 by Library user on 07 September 2018

The results are consistent for the one- and the two-parameter fits. All BL Lacs are radio-selected and, moreover, belong to the class of objects with low-energy cut-offs of the spectral energy distribution (Giommi & Padovani 1994). Apart from one, all BL Lacs for which spectral information could be obtained are also included in the analysis of the 1-Jy BL Lac sample by Urry et al. (1996). Our average photon index is steeper than that of the total 1-Jy sample ($\langle\Gamma\rangle \sim 2.2$: Urry et al. 1996), but still consistent within the errors.

Radio galaxies exhibit harder X-ray spectra on average compared with quasars and BL Lac objects. From the 17 galaxies with spectral information available, we find $\langle\Gamma\rangle \approx 1.7$. The result is consistent with the average spectral indices for much larger samples of radio galaxies presented in Brinkmann et al. (1994, 1995).

The dependence of the quasar soft X-ray photon index on redshift is shown in Fig. 7 for sources with well-determined spectra, i.e. $\Delta\Gamma < 0.5$. According to Schartel et al. (1996), it is due to the fact that the *ROSAT* PSPC samples the X-ray spectrum at increasingly higher energies in the rest frame of the source as the redshift increases. As a consequence, the steep soft X-ray component is shifted out of the PSPC energy range and the generally flatter X-ray component at higher energies starts to dominate in the observed 0.1–2.4 keV range. This effect is also seen in the present sample of flat-spectrum quasars. A Spearman rank correlation test gives a probability of $P = 0.0035$ that the observed correlation occurs by chance. A weighted least-squares regression analysis gives $\Gamma = (2.33 \pm 0.08) - (0.33 \pm 0.06) \times z$. The result is perfectly consistent with the findings of Brinkmann et al. (1997a) for a much larger, but inhomogeneous, sample of flat-spectrum quasars. Interestingly, the dependence on redshift is slightly steeper for flat-spectrum quasars than for steep-spectrum quasars [$\Gamma = (2.29 \pm 0.08) - (0.19 \pm 0.11) \times z$]. This may be interpreted in terms of a selection effect. In flux-limited samples only the most luminous objects are included at any given redshift (Malmquist bias). For flat-spectrum radio samples, this means that at higher redshifts one preferentially selects objects for which the spectral energy distribution is dominated by beamed emission from the radio jet. Therefore it is the combination of the intrinsically higher energies sampled with the PSPC observations and the increasing contribution of the flat X-ray component from the jet that produce a steeper gradient of the photon index with redshift compared with steep-spectrum quasars, for which the latter effect is less important.

As already mentioned, the photon indices of flat-spectrum quasars are also correlated with the radio spectral index between 2.7 and 5 GHz. This correlation is illustrated by Fig. 8 for quasars with well-determined photon indices ($\Delta\Gamma < 0.5$). The flatter or the more inverted is the radio continuum, the harder is the soft X-ray spectrum. The correlation holds for photon indices determined at fixed Galactic $N_{\rm H}$ as well as for those determined with free absorption. A Spearman rank correlation analysis gives a probability of $P = 0.040$ that the observed correlation occurs by chance. A weighted least-squares regression analysis gives $\Gamma = (2.02 \pm 0.05) - (0.50 \pm 0.19) \times \alpha$. We note that Brinkmann et al. (1997a) find no significant correlation of Γ with α for flat-spectrum quasars, which may be due to the fact that we constrain our analysis to objects with well-determined photon indices (almost half of them from fits to data obtained in pointed PSPC observations).

Within the framework of orientation-dependent unification scenarios for radio-loud AGN (Urry & Padovani 1995 and references therein), steep- and flat-spectrum radio sources are the increasingly aligned counterparts of Fanaroff–Riley type II radio galaxies (Fanaroff & Riley 1974). Therefore the radio spectral index roughly indicates the orientation of the source with respect to the line of sight. In this model the observed correlation between X-ray and radio spectral index can be interpreted as being due to a beamed X-ray component with a harder spectrum, which is directly related to the radio emission from the radio core and which dominates the total X-ray emission at small angles to the line of sight.

4.5 Luminosity correlations

To investigate whether the emission at two different frequencies is *intrinsically* related, we seek for correlations in luminosity–luminosity diagrams. It is often stated that observed luminosity correlations are significantly affected by redshift effects, i.e. the correlation appears in absolute luminosities even for uncorrelated fluxes, because the (narrow) flux range is stretched out by a large distance factor. Feigelson & Berg (1983) invert this argument by pointing out that objects will not be detected in small flux ranges at two frequencies *unless* the luminosities are intrinsically related. Generally, the more distant objects will exhibit flux upper limits in one band if no relationship exists. If these upper limits are properly taken into account, intrinsic relationships can be recovered from luminosity–luminosity diagrams (Feigelson & Berg 1983). We further note that intrinsic relationships cannot be determined from flux–flux diagrams anyway, unless the underlying relationship is linear (e.g. Kembhavi, Feigelson & Singh 1986).

The radio, optical and X-ray luminosities of our sample were calculated assuming $H_0 = 50$ km s^{-1} Mpc^{-1} and $q_0 = 0.5$. For the *K*-correction we used in the radio band the radio spectral indices between 2.7 and 5 GHz as given in Drinkwater et al. (1997). For the X-ray luminosity the photon indices for Galactic absorption as derived in Section 3.3 were used if the error was smaller than 0.5. Otherwise the average values for quasars, galaxies and BL Lac objects were applied. The optical luminosity was corrected for Galactic reddening and *K*-corrected to 4400 Å with a spectral index of $\alpha = -0.5$.

Correlation and regression analyses were performed with ASURV (Rev.1.3: La Valley, Isobe & Feigelson 1992), which is particularly designed for censored data. For the correlation analysis we applied the modified Kendall τ, and for the regression analysis we used the parametric EM algorithm from this software package. To investigate the influence of redshift on the correlations, we performed a partial correlation analysis using the procedure described in Akritas & Siebert (1996), which allows us to determine the partial correlation coefficient in the presence of upper limits and to calculate the significance of this corrected correlation coefficient. The results from this analysis are summarized in Table 5. For completeness we give the parameters for both the $L_{\rm o} - L_{\rm x}$ and the $L_{\rm r} - L_{\rm x}$ correlations, although we will discuss only the latter in detail.

In Fig. 9 we show the relation between radio and X-ray luminosities for quasars, galaxies and BL Lac objects. For all three object classes the X-ray and the radio luminosities are obviously correlated with each other. The slope of the regression line for quasars is $a_1 = 0.61 \pm 0.08$, which is consistent with the findings of Brinkmann et al. (1997a) for the inhomogeneous sample of X-ray detected flat-spectrum quasars from the Véron–Véron catalogue. They find $a_1 = 0.72 \pm 0.11$ using orthogonal distance regression, which is superior to simple least-squares methods for theoretical reasons, but which is unfortunately not available for censored data. We note that neglecting the upper limits only slightly affects the slope of the correlation. The partial correlation analysis confirms that the observed relation is not due to a common dependence of both luminosities on redshift. Although the probability for the

Downloaded from https://academic.oup.com/mnras/article-abstract/301/1/261/1058213 by Library user on 07 September 2018

Table 5. Results of the correlation and regression analysis.

(1)	(2)	N (3)	N_{UL} (4)	τ (5)	P_{12} (6)	a_0 (7)	a_1 (8)	a_0' (9)	a_1' (10)	$\tau_{xy.z}$ (11)	$P_{12.3}$ (12)
quasars	L_r–L_x	226	110	0.22	$<10^{-7}$	22.7±2.4	0.66±0.07	18.1±2.1	0.80±0.06	0.16	$9.6\cdot10^{-7}$
	L_o–L_x	225	109	0.22	$<10^{-7}$	29.7±1.9	0.50±0.06	26.1±1.8	0.63±0.06	0.18	$1.2\cdot10^{-7}$
galaxies	L_r–L_x	33	9	0.45	$0.8\cdot10^{-4}$	14.4±4.5	0.90±0.14	11.9±2.9	0.99±0.09	0.22	0.048
	L_o–L_x	33	9	0.16	0.16	...	...	...	...	...	...
BL Lacs	L_r–L_x	10	0	0.67	0.012	13.7±5.4	0.93±0.16	...	...	0.41	0.276
	L_o–L_x	10	0	0.78	$0.4\cdot10^{-2}$	14.8±4.3	0.99±0.14	...	...	0.61	0.201

Column. (1) Object class. (2) Type of correlation (independent – dependent variable). (3) Number of sources used. (4) Number of upper limits. (5) Kendall's τ correlation coefficient. (6) Probability that the observed correlation occurs by chance from intrinsically uncorrelated data according to Kendall's τ test. (7) and (8) Parameters of the regression line $y = a_0 + a_1 \cdot x$. (9) and (10) Same as (7) and (8), but only detected sources are taken into account. (11) Partial correlation coefficient, with redshift effects eliminated. (12) Significance of the partial correlation coefficient.

observed correlation to occur by chance increases if redshift effects are taken into account, the correlation is still highly significant ($P = 9.6 \times 10^{-7}$).

Compared with quasars, the correlation between radio and X-ray luminosities seems to be steeper for galaxies and BL Lac objects. In the case of galaxies, the slope of the correlation is consistent with previous findings within the mutual uncertainties (Fabbiano et al. 1984; Brinkmann et al. 1995). However, an interpretation of the relation between total radio and X-ray luminosities in terms of nuclear activity is hampered by contaminating X-ray emission from various galactic processes or surrounding clusters of galaxies in many of the radio galaxies. The spatial resolution in the RASS generally does not allow one to isolate the AGN contribution to the total X-ray emission.

The slope of the regression line for the BL Lac objects is consistent with unity, which might argue for a direct physical relation between the radio and the X-ray emission. Since the radiation in both wavebands is thought to be dominated by the relativistic jet (e.g. Kollgaard 1994), this would not be surprising. However, the partial correlation analysis indicates that the correlation for BL Lac objects is strongly influenced by selection effects and is no longer significant, if redshift effects are taken into account. On the other hand, we note that the number of objects is rather low. Therefore the results of statistical analyses have to be interpreted with caution.

5 IS THERE EVIDENCE FOR DUST-REDDENED QUASARS?

Based on the large scatter in the $B_J - K$ colours of the quasars in the present sample, Webster et al. (1995) claimed that there might be a large population of previously undetected, red quasars. They suggested that this reddening is due to dust intrinsic to the quasars. In this section we will investigate if there are any arguments from the X-ray data in support of this hypothesis. A discussion of the results will be presented in Section 6.

5.1 Dust extinction and expected X-ray absorption

If the optical reddening is due to dust, it is expected that the reddest quasars are also intrinsically absorbed in soft X-rays. Using Galactic gas-to-dust ratios [i.e. $N_{H1+H_2} = 5.8 \times 10^{21} E(B-V)$ cm^{-2}: Bohlin, Savage & Drake 1978], the extinction coefficients $R_\lambda = A_\lambda / E_{B-V}$ from Seaton (1979) and the energy-dependent X-ray absorption coefficients given by Morrison & McCammon (1983), we can estimate the influence of the absorption by cold gas associated with the dust on the soft X-ray flux for a given *observed* extinction $A_{B,obs}$. For example, $A_{B,obs} = 5$ corresponds to an intrinsic N_H of $\sim 7 \times 10^{21}$ cm^{-2} for local objects, which reduces the *observed* X-ray flux in the total 0.1–2.4 keV energy band by more than a factor of 3. For redshifts of $z \approx 1.3$, which is the average redshift of the present quasar sample, an observed optical extinction of $A_{B,obs} = 5$ corresponds to a rest-frame N_H of $\sim 3 \times 10^{21}$ cm^{-2}, which reduces the observed 0.1–2.4 keV flux still by a factor of ~ 1.4.

We further note that the decrease of the observed optical (4400 Å) flux by dust extinction, which is given by $\approx 10^{-0.4 A_B}$, generally is larger than the corresponding decrease of the soft X-ray flux caused by absorption by cold gas associated with the dust, in particular for higher redshifts. For example, an *intrinsic* extinction of $A_B = 2$ at a redshift of $z = 1$ reduces the *observed* 4400-Å flux by a factor of 50, whereas the *observed* 0.1–2.4 keV flux is only reduced by a factor of ≈ 1.3. This point is important in the discussion of the $\log(f_x/f_o)$ distribution in Section 5.5.

5.2 Detection probability

In a first step we compared the shape of the optical continuum for the detected quasars with those for the upper limit sources. The result is shown in Fig. 10 for the total sample. The optical continuum is parametrized by the power-law slope α_{opt} ($f_\nu \propto \nu^\alpha$), which is given in Francis et al. (in preparation) for 181 sources of the sample. They find a correlation between the optical slopes and the $B_J - K$ colours. The optical slope can therefore be used to parametrize the redness of the optical continuum, which in turn is a measure of the amount of dust present in the source, if one follows the interpretation of Webster et al. (1995).

The values of α_{opt} show a large scatter and range from -4 to $+1.5$, but nevertheless the distributions for detections and upper limits look very similar. In particular, the upper limits do not cluster towards red optical continua. This is confirmed by a KS test, which gives $P = 0.83$, i.e. if we reject the null-hypothesis that the two distributions are drawn from the same parent population, the error probability is 83 per cent. Confining the sample to low redshifts ($z < 1.0$), where the absorption effect on the X-ray flux should be most easily detectable, this probability is even higher (97.3 per cent). We therefore conclude that intrinsic absorption by gas/dust is not the main reason for a source not to be detected in soft X-rays, and confirm our conclusion in Section 4.1 that distance is the most important parameter.

Downloaded from https://academic.oup.com/mnras/article-abstract/301/1/261/1058213 by Library user on 07 September 2018

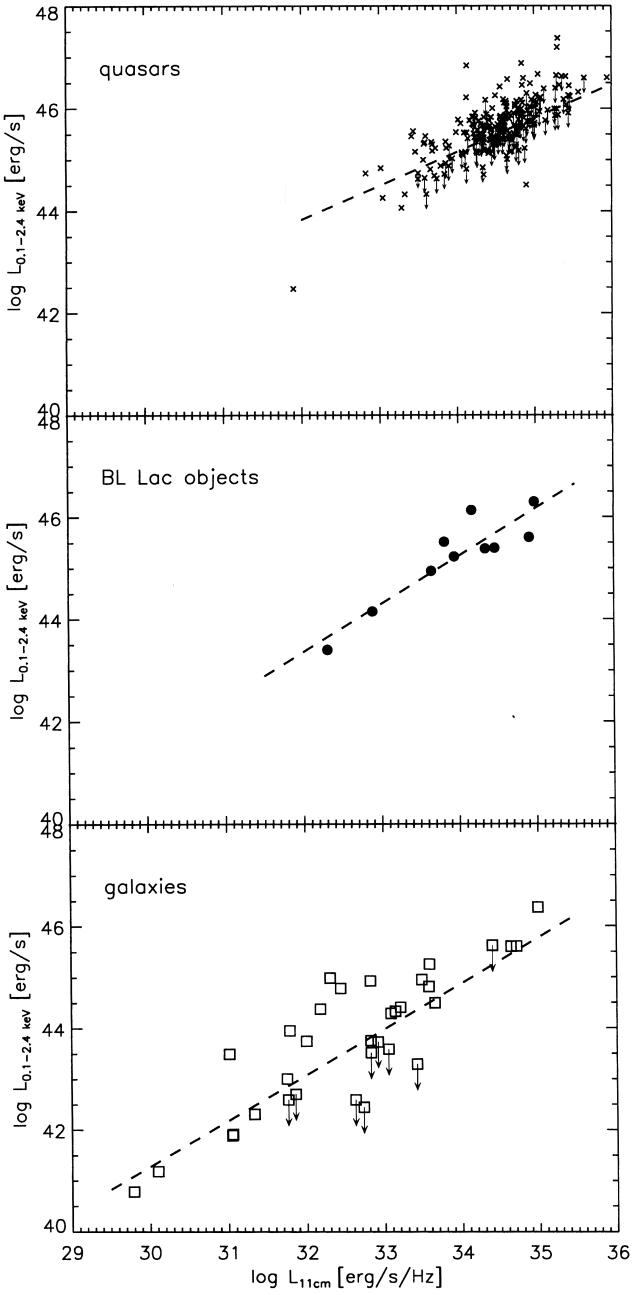

Figure 9. Soft X-ray luminosity of quasars, BL Lac objects and galaxies as a function of the total 2.7-GHz (11-cm) radio luminosity. The results of the regression analysis including the upper limits are indicated by the dashed lines (cf. Table 5).

5.3 X-ray luminosities

As shown in Section 5.1, absorption by cold gas associated with the inferred amounts of dust can have a significant effect on the soft X-ray flux and hence the observed X-ray luminosity. In Fig. 11 we compare the soft X-ray luminosity distributions for 'stellar' sources with an optical continuum slope $\alpha_{opt} > -1$ (hatched) with those having $\alpha_{opt} < -1$ (thick line). For clarity, only the detected sources are shown. In the statistical analysis, however, we included the upper limits.

For low-redshift sources the luminosity distributions are clearly different (upper panel). On average, the optically 'red' sources have

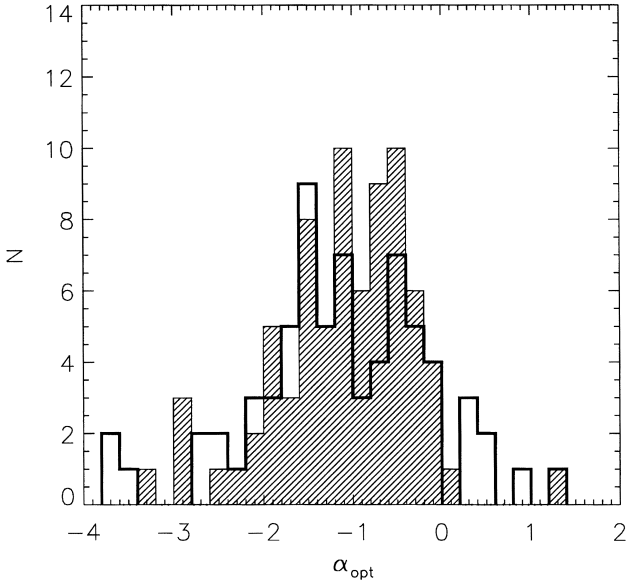

Figure 10. Comparison of the power-law indices of the optical continuum for X-ray detections (solid line) and upper limits (hatched). The two distributions are statistically indistinguishable.

X-ray luminosities that are a factor of 2–3 lower than those of their 'blue' counterparts. Using Gehan's generalized Wilcoxon test as implemented in ASURV, we get $P = 0.0082$, i.e. the probability for erroneously rejecting the null hypothesis that the distributions are the same is only 0.8 per cent. We further note that the redshift distributions of the low-redshift 'red' and 'blue' subsamples are indistinguishable ($P = 0.42$). The effect almost completely disappears for sources at higher redshifts ($z > 1$; lower panel). The soft X-ray luminosity distributions for the two object classes are statistically indistinguishable ($P = 0.69$).

This kind of redshift dependence is the expected signature of intrinsic X-ray absorption by cold gas associated with the dust

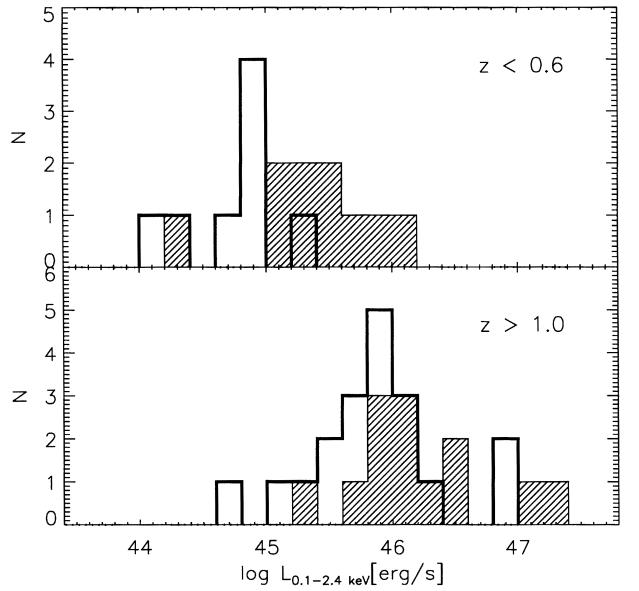

Figure 11. The soft X-ray luminosity distributions for detected sources with $\alpha_{opt} > -1$ (hatched) and $\alpha_{opt} < -1$ (thick line). In the upper panel only low-redshift 'stellar' sources are considered ($z < 0.6$), whereas the high-redshift sources ($z > 1$) are shown in the lower panel.

Downloaded from https://academic.oup.com/mnras/article-abstract/301/1/261/1058213 by Library user on 07 September 2018

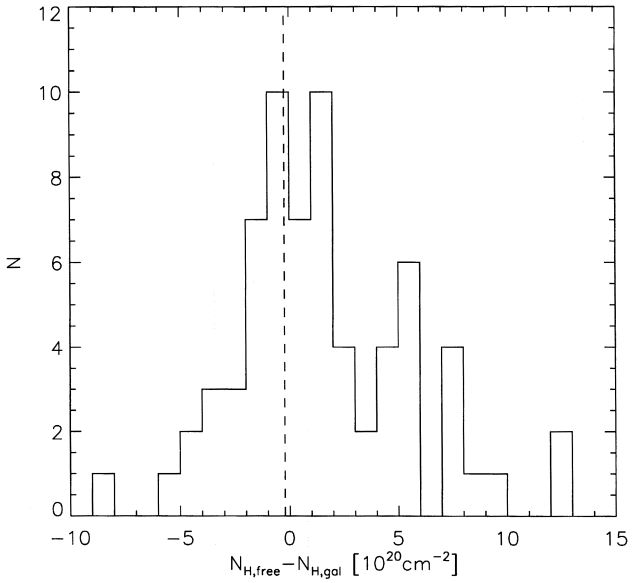

Figure 12. Histogram of the difference between the X-ray derived N_H value from the two-parameter fits and the Galactic N_H value. The weighted average (dashed line) is consistent with zero excess absorption.

inferred from the observed optical reddening. In Section 5.1 we have shown that the effect of the deduced amount of cold gas on the soft X-ray flux decreases with redshift.

However, there might be selection effects at work, which could lead to a similar result. In particular, the low-redshift sources, although all of them appear stellar on the UK Schmidt Telescope (UKST) and Palomar Optical Sky Survey (POSS) I plates, might still be contaminated by galaxies or BL Lac objects. Galaxies and BL Lac objects are known to have redder optical continua and lower X-ray luminosities than quasars (Brinkmann et al. 1995). We therefore checked, in data bases, literature and our own optical data, whether any of the low-redshift 'red' sources actually have to be classified as a galaxy or a BL Lac object. First of all, no source shows a strong galaxy continuum in the spectrum as presented in Francis et al. (in preparation). Only for three sources does the identification seem questionable according to the NASA/IPAC Extragalactic Data base (NED). The sources 1020−103 and 1034−293 are classified as BL Lacs. However, strong emission lines have been reported for these sources (Falomo, Scarpa & Bersanelli 1994; Falomo 1996). These sources should therefore be considered as quasars instead of BL Lac objects. The third source, 0003−066, is listed as a radio galaxy and BL Lac candidate in NED, but Stickel, Meisenheimer & Kühr (1994) classify this source as a quasar based on several weak emission lines.

We conclude that the contamination of the low-redshift 'red' sources by low-luminosity galaxies and BL Lac objects cannot explain the observed difference in the soft X-ray flux distributions.

5.4 Soft X-ray spectra

Next we investigate if the influence of dust-associated absorption can be seen in the soft X-ray spectra of the sources directly. If excess absorption exists, it should lead to a substantially higher value of N_H than the Galactic one in the two-parameter fits. Again, the effect should be strongest at low redshifts, since the required amounts of intrinsic N_H to produce an observed extinction of A_B may be too low to be significantly detected in high-redshift sources. In Fig. 12 we show the distribution of the difference $\Delta N_H = N_{H,free} - N_{H,gal}$ between the derived N_H and the Galactic N_H value for the quasars in the sample. There seems to be an asymmetry towards positive ΔN_H values. However, a more detailed analysis shows that most of the high ΔN_H values come from spectral parameters derived from hardness ratios and the error bars are very large. In addition, it is known that the hardness ratio technique leads to systematically higher N_H values for weak sources (Yuan, Brinkmann & Siebert 1998). The weighted average of the ΔN_H distribution is $\langle \Delta N_H \rangle = (-0.22 \pm 0.68) \times 10^{20}$ cm^{-2}, which indicates that excess absorption is not a general feature. In particular, the sources with very red optical continua show no evidence for systematically higher absorption in soft X-rays.

Only six sources show significantly higher observed $N_{H,free}$ compared with the Galactic N_H value (0438−436, 1148−001, 1402+044, 2126−158, 2223−052 and 2351−154). All of them have high redshifts in the range $1.40 < z < 3.27$. A detailed analysis of the excess X-ray absorption has already been published for 0438−436 (Cappi et al. 1997), 2126−158 (Elvis et al. 1994) and 2351−154 (Schartel et al. 1997). The required amounts of intrinsic N_H range from 1.7×10^{21} to 1.2×10^{22} cm^{-2} for these sources. If we again assume Galactic gas-to-dust ratios, the associated dust extinction in the (observed) B band will be much higher than the maximum value ($\approx$5 mag) observed by Webster et al. (1995). For three of these sources (1402+044, 2126−158 and 2351−154), optical continuum slopes are available and they do not indicate a particularly red continuum ($\alpha_{opt} = -1.438$, -0.588 and -0.297, respectively). Several explanations for this contradictory result are conceivable, and they are briefly discussed in Section 6.

5.5 Log (f_x/f_o) distribution

It has been argued by Webster et al. (1995) that the large dispersion in the X-ray to optical flux ratios for X-ray selected quasars found by Stocke et al. (1991) is indicative of variable dust extinction. This has been criticized by Boyle & di Matteo (1995), who show that the observed scatter of the X-ray to optical flux ratio in their sample of X-ray selected quasars is much smaller than expected if variable extinction is important.[3]

In Fig. 13 we show the flux ratio $\log(f_x/f_o)$ as a function of redshift z for the present sample. f_x is the monochromatic X-ray flux at 1 keV in erg cm^{-2} s^{-1} Hz^{-1}, which is derived from the flux in the total *ROSAT* energy band assuming the average spectral parameters derived in Section 4.4. f_o is the observed flux at 4400 Å, calculated from the B_J magnitude and corrected for Galactic reddening according to the formula (Giommi, Ansari & Micol 1995)

$$f_o = 10^{-0.4 \times B_J + 0.08/\sin(|b|) - 19.377},$$

where b is the Galactic latitude of the source. In the lower right-hand corner of Fig. 13 we show a conservatively calculated error bar, assuming a 25 per cent error of the X-ray flux and an uncertainty of the optical magnitudes of $\Delta m = 0.5$ (Drinkwater et al. 1997). Since the optical and the X-ray data were not taken simultaneously, we also include the expected B-band variability of $\sigma(B) = 0.3$ mag for a typical quasar of our sample and the rest-frame ~20-yr baseline between the optical and the X-ray measurements (Hook et al. 1994).

A decrease of $\log(f_x/f_o)$ with redshift up to $z \sim 2.5$ is apparent

[3] The authors base their analysis on the absorption coefficients in the optical and X-ray bands, thereby neglecting the different column densities of absorbing material in the two wavebands, i.e. dust in the optical and neutral gas in X-rays. The difference is important, in particular at low redshifts (cf. Section 5.1).

Downloaded from https://academic.oup.com/mnras/article-abstract/301/1/261/1058213 by Library user on 07 September 2018

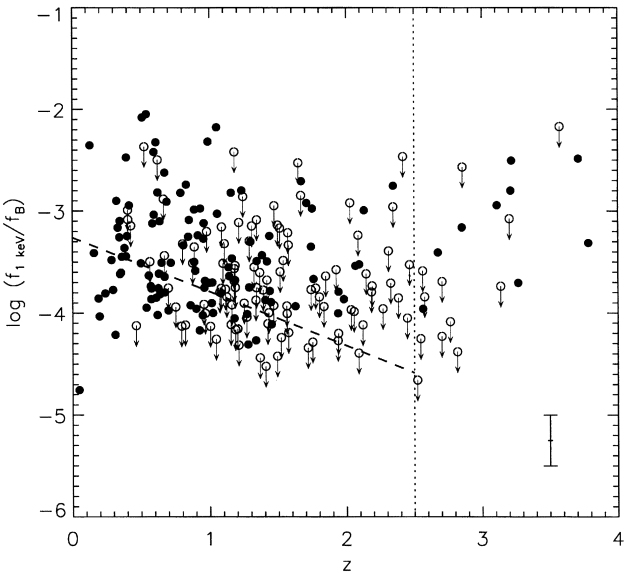

Figure 13. The flux ratio $\log(f_x/f_o)$ as a function of redshift z for quasars. Open circles plus arrows indicate X-ray upper limits. The dashed line represents the best regression line for $z < 2.5$ objects including the upper limits. The vertical dotted line is drawn at $z = 2.5$ for illustrative purposes. In the lower right-hand corner we show a conservatively estimated typical error bar.

from Fig. 13, and it turns out to be highly significant using Spearman's ρ correlation test as implemented in ASURV ($\rho_{sp} = -0.40$ for 204 data points). However, this trend is mainly caused by the different spectral indices at optical and X-ray energies, which cause a spurious correlation of the form $\log(f_x/f_o) \propto (1+z)^{-\alpha_x+\alpha_{opt}}$. Indeed, using ASURV to determine the best regression line, we get $\log(f_x/f_o) = (-3.26 \pm 0.12) - (0.53 \pm 0.10) \times z$, if we only consider objects with $z < 2.5$. The slope is roughly consistent with the difference in the average spectral indices in the X-ray and the optical regimes.

Interestingly, the trend with redshift seems to be inverted at redshifts greater than ~2.5, which is mainly mimicked by a deficit of high-redshift sources with low $\log(f_x/f_o)$ values.[4]

Most likely, various effects combine to result in an apparent deficit of sources with low values of $\log(f_x/f_o)$ at higher redshifts. First, the X-ray emission could be enhanced, for example by relativistic beaming. This hypothesis is supported by the generally very flat or inverted radio spectra of these objects and their high core dominance. Basically, this is a selection effect of the radio sample. At high redshifts only the most powerful (and hence probably beamed) objects make it into the flux-limited sample. Further, the optical flux may be reduced, because the Lyα edge shifts into the B band for $z > 2.5$. Finally, we note that a positive correlation is also expected in the case of dust extinction, because the effect of dust on the optical continuum of high-redshift sources is much stronger than that of the associated neutral gas on the X-ray emission (cf. Section 5.1). Some of these high-redshift objects do show significant intrinsic absorption in X-rays (see previous section), and they are optically dull with $B_J > 21$ mag. Therefore it cannot be excluded that their high X-ray to optical flux ratios are at least in part due to dust extinction.

Analogously to Boyle & di Matteo (1995), we investigate the dispersion in the distribution of the flux ratio $\log(f_x/f_o)$, which can be used at least to derive upper limits on the amount of dust obscuration. As has been shown in Section 5.1, the effect of intrinsic gas and dust on the observed optical flux is much stronger than on the X-ray flux, in particular at higher redshifts. To first order, the observed spread in $\log(f_x/f_o)$ might therefore be almost completely attributed to variations in f_o arising from dust extinction.

If we apply the 'detections and bounds' (DB) method of Avni et al. (1980) in order to account properly for upper limits, we get $\langle \log(f_x/f_o) \rangle = -3.87$ and $\sigma[\log(f_x/f_o)] = 0.70$, which is significantly larger than the Boyle & di Matteo value ($\sigma \sim 0.4$). The derived $\pm 1\sigma$ width of the $\log(f_x/f_o)$ distribution corresponds to a variation in f_x/f_o by a factor of ~25. Assuming that all of the scattering is due to dust extinction (and thus neglecting other effects like X-ray variability, measurements errors, etc.), this gives an upper limit to the amount of reddening in the observed B band of < 3.5 mag. This is slightly below the maximum values claimed by Webster et al. (1995), but, since the estimate is based on the FWHM of the $\log(f_x/f_o)$ distribution, the observed maximum value of $A_B = 5$ might still be consistent with the observed scatter.

Clearly, the observed scatter in $\log(f_x/f_o)$ for the Parkes quasars cannot be regarded as clear evidence for the presence of dust. We may conclude, however, that it also does not rule out the dust extinction hypothesis, as has been claimed from the corresponding analysis of X-ray and optically selected samples, which exhibited a much smaller scatter in $\log(f_x/f_o)$ (Boyle & di Matteo 1995).

6 DISCUSSION

One of the main aims of this study was to look for any evidence from the X-ray data in favour of or against the hypothesis of Webster et al. (1995) that the observed red continua of many of the Parkes flat-spectrum quasars are due to dust extinction. Our results can be summarized as follows.

First of all, none of the observed X-ray properties is in contradiction to the dust hypothesis. On the other hand, it is also difficult to prove the presence of dust from the X-ray data, because the argument is always an indirect one.

The strongest indication for dust comes from the significantly lower X-ray luminosities of the low-redshift 'stellar' objects with red optical continua, as compared with their blue counterparts. The difference vanishes for higher redshifts. This is expected, if neutral gas associated with the dust is responsible for the soft X-ray absorption and the corresponding reduction of the X-ray flux, because, for high redshifts, the X-ray observation samples increasingly higher energies in the rest-frame spectrum of the source, and the column density of neutral gas associated with the dust inferred from optical reddening is too low to affect the X-ray flux significantly at these relatively high rest-frame energies. Therefore no difference in the luminosity distributions for red and blue objects is measurable any more. For the low-redshift sources, the observed difference in the average X-ray luminosity is about a factor of 2, which is consistent with the optical data. We have further shown that the observed luminosity difference is not due to a contamination of the 'stellar' sources of our sample with low luminosity 'red' sources like BL Lac objects or radio galaxies. We conclude that dust-associated absorption represents a viable explanation for the observed effect.

In view of this result, it seems surprising that we do not find any

[4] Note that the quasar with the highest upper limit on $\log(f_x/f_o)$ (PKS 2215+02, $z = 3.572$) has been detected in a recent pointed *ROSAT* High Resolution Imager (HRI) observation [Siebert & Brinkmann 1998]. The deduced X-ray flux is only slightly below the quoted upper limit from the RASS.

Downloaded from https://academic.oup.com/mnras/article-abstract/301/1/261/1058213 by Library user on 07 September 2018

difference in the X-ray detection probability for the red and the blue stellar objects. Since the observed X-ray flux should be reduced by absorption for the reddened sources, the fraction of upper limits would also have been expected to be higher among these sources. As shown in Section 5.2, this is obviously not the case. However, in Section 4.1 we concluded that distance is the most important factor, that determines the detection probability in soft X-rays, and the absorption effect as discussed above is not strong enough to dominate over distance. Indeed, for a given intrinsic luminosity and reasonable amounts of cold gas, the observed soft X-ray flux is at most reduced by a factor of 3 because of absorption, whereas it has already declined by a factor of $\sim$3.5 when the source is shifted from $z = 0.1$ to 0.2.

Since many of the spectral parameters were determined from the hardness ratios, which usually result in relatively large uncertainties, it is impossible to derive any stringent constraints on the amount of dust-associated absorption from the X-ray spectra of the Parkes quasars. We find only six objects with a significant $\Delta N_{\rm H} = N_{\rm H,free} - N_{\rm H,gal} > 0$, however, all of them at high redshift. Thus the implied amounts of dust (again assuming Galactic gas-to-dust ratios) would be much higher than observed in the optical spectra. This apparent discrepancy has already been noted previously (e.g. Elvis et al. 1994), and several solutions have been proposed. First of all, all estimates of the expected amount of X-ray absorption (or optical reddening) are based on the assumption of Galactic gas-to-dust ratios, and it is not at all certain, whether this assumption is still valid at high redshifts. Indeed, Pei, Fall & Bechtold (1991) show that the gas-to-dust ratio is at least 10 times higher in damped Lyα systems. Thus a high neutral gas column may not necessarily imply a correspondingly large dust column, and therefore significant X-ray absorption may not be accompanied by a large optical extinction. Similarly, the metal abundances could be reduced at large redshifts, which also is indicated by the properties of damped Lyα systems (e.g. Turnshek et al. 1989; Meyer & Roth 1990).

Also, finally the observed large scatter in the $\log(f_{\rm x}/f_{\rm o})$ distribution does not allow us to draw any firm conclusions about the amount of dust present in radio-loud quasars. In particular, the observed deficit of high-redshift sources with low $\log(f_{\rm x}/f_{\rm o})$ ratios is most likely not due to dust extinction, because the optical continua of the high-redshift sources are not particularly red. We note, however, that a large observed scatter is also not inconsistent with the dust hypothesis as was claimed previously based on the analysis of optically and X-ray selected samples.

One explanation for the limited evidence for dust-associated absorption in the X-ray data could be that the large spread in the $B_{\rm J}-K$ colours reported by Webster et al. (1995) is not due to dust. Many alternative suggestions have been made to explain the observed $B_{\rm J}-K$ values, such as an intrinsically red optical continuum, a host galaxy contribution (Benn et al. 1998) or relativistic beaming (Srianand & Kembhavi 1997). It is beyond the scope of this paper to discuss the possible origins of the observed $B_{\rm J}-K$ colours. This will be done in a future paper (Francis et al., in preparation). Here we only note that detailed investigations of the optical spectra of many of the red sources show that an intrinsic origin for the red colours gives the best fit to the spectra of around half of the red sources, but the remainder, including many of the reddest sources, do show signs of dust reddening (Francis et al., in preparation). A similar result has been reported by Puchnarewicz & Mason (1998), who find evidence for reddening by dust among those *ROSAT* International X-ray Optical Survey (RIXOS) AGN with very red optical continua.

If one accepts the dust hypothesis, then why does the neutral gas associated with the dust not show up more clearly in the soft X-ray regime? Various explanations are conceivable. First of all, it has already been noted that all estimates are based on the assumption that the gas-to-dust ratio in all quasars is the same as that in our Galaxy. If the gas-to-dust ratio is lower, the observed dust extinction is not accompanied by a large neutral gas column and the corresponding X-ray absorption might not be measurable given the limited sensitivity of the present data. Secondly, the ionization state of the gas associated with the dust is unknown. If the gas is ionized, its X-ray opacity is reduced and it will therefore allow for larger amounts of dust without strongly affecting the soft X-ray emission. So-called 'dusty warm absorbers' have recently been claimed to exist in a couple of sources, e.g. IRAS 1334+2438 (Brandt, Fabian & Pounds 1996) and NGC 3786 (Komossa & Fink 1997). Clearly, the quality of the available X-ray spectra of the sources presented in this paper is not sufficient to constrain the ionization state of the absorbing gas.

High-quality X-ray spectra are needed to quantify directly the amount of dust probably present in optically red quasars by measuring the carbon absorption edge at $\sim$0.3 keV. These are currently not available, but future X-ray missions like *XMM* and *AXAF*, which combine a large effective area with high energy resolution down 0.2 keV, should be able to provide the necessary data.

7 CONCLUSIONS

Using *ROSAT* All–Sky Survey data and pointed PSPC observations, we have determined the X-ray properties of all 323 objects from the Parkes sample of flat-spectrum radio sources as defined in Drinkwater et al. (1997). The results are as follows.

(i) 163 sources were detected at the 3σ level. For the remaining 160 sources, 2σ upper limits to the soft X-ray flux were determined.

(ii) Using a hardness ratio technique and explicit fits to the data, we determined the soft X-ray spectra of 115 sources. The average power-law photon index for flat-spectrum quasars is $\langle\Gamma\rangle = 1.95 \pm 0.13$, slightly flatter ($\Delta\Gamma \sim 0.2$) than for 'ordinary' radio-loud quasars. The average photon index for BL Lac objects is $\langle\Gamma\rangle = 2.40^{+0.12}_{-0.31}$, whereas radio galaxies generally display harder soft X-ray spectra ($\langle\Gamma\rangle = 1.70 \pm 0.23$).

(iii) We confirm the inverse correlation of the spectral index with redshift for radio-loud quasars. We have also found a significant inverse correlation of the photon index with the radio spectral index between 2.7 and 5 GHz, which is in accord with current orientation-dependent unification schemes for radio-loud AGN.

(iv) Correlations of X-ray luminosity with total radio luminosity have been found for quasars, galaxies and BL Lac objects. Partial correlation analyses indicate that a redshift effect is negligible for quasars and galaxies, whereas it might influence the correlation for BL Lacs.

The question of whether intrinsic dust is the origin of the observed red optical continua of many of the quasars of the sample cannot be unambiguously answered on the basis of the X-ray properties presented. Nevertheless, it is tempting to interpret the redshift dependence of the difference in the observed X-ray luminosities for optically red and blue sources in terms of dust-associated absorption. However, firm conclusions on the basis of current X-ray data are hampered by the fact that all arguments rely on implicit assumptions, which may not be valid in general, such as

Downloaded from https://academic.oup.com/mnras/article-abstract/301/1/261/1058213 by Library user on 07 September 2018

Galactic gas-to-dust ratios in quasars and a low ionization state of the X-ray absorbing gas associated with the dust.

ACKNOWLEDGMENTS

The *ROSAT* project is supported by the Bundesministerium für Forschung and Technologie (BMBF). We thank our colleagues from the *ROSAT* group for their support. This research has made use of the NASA/IPAC Extragalactic Data Base (NED), which is operated by the Jet Propulsion Laboratory, California Institute of Technology, under contract with the National Aeronautics and Space Administration.

REFERENCES

Akritas M. A., Siebert J., 1996, MNRAS, 278, 919
Avni Y., Soltan A., Tananbaum H., Zamorani G., 1980, ApJ, 238, 800
Baker J. C., Hunstead R. W., 1995, MNRAS, 277, 553
Benn C. R., Vigotti M., Carballo R., Gonzalez-Serrano J. I., Sánchez S. F., 1998, MNRAS, 295, 451
Bohlin R. C., Savage B. D., Drake J. F., 1978, ApJ, 224, 132
Bolton J. G., Savage A., Wright A. E., 1979, Aust. J. Phys., Astrophys. Suppl., 46, 1
Boyle B. J., di Matteo T., 1995, MNRAS, 277, 63P
Brandt W. N., Fabian A. C., Pounds K. A., 1996, MNRAS, 278, 326
Brinkmann W., Siebert J., Boller T., 1994, A&A, 281, 355
Brinkmann W., Siebert J., Reich W., Fürst E., Reich P., Voges W., Trümper J., Wielebinski R., 1995, A&AS, 109, 147
Brinkmann W., Yuan W., Siebert J., 1997a, A&A, 319, 413
Brinkmann W. et al., 1997b, A&A, 323, 739
Brunner H., Friedrich P., Zimmermann H.-U., Staubert R., 1992, in Brinkmann W., Trümper J., eds, MPE Report 235, X-ray emission from active galactic nuclei and the cosmic X-ray background. MPE, Garching, p.198
Cappi M., Matsuoka M., Comastri A., Brinkmann W., Elvis M., Palumbo G. G. C., Vignali C., 1997, ApJ, 478, 492
Condon J. J., Broderick J. J., Seielstad G. A., 1989, AJ, 97, 1064
Dickey J. M., Lockman F. J., 1990, ARA&A, 28, 215
Drinkwater M.J. et al., 1997, MNRAS, 284, 85
Elvis M., Fiore F., Wilkes B., McDowell J., 1994, ApJ, 422, 60
Fabbiano G., Miller L., Trinchieri G., Longair M., Elvis M., 1984, ApJ, 277, 195
Falomo R., 1996, MNRAS, 283, 241
Falomo R., Scarpa R., Bersanelli M., 1994, ApJS, 93, 125
Fanaroff B. L., Riley J. M., 1974, MNRAS, 167, 31P
Feigelson E. D., Berg C., 1983, ApJ, 269, 400
Giommi P., Padovani P., 1994, MNRAS, 268, 51P
Giommi P., Ansari S.G., Micol A., 1995, A&AS, 109, 267
Green P.J. et al., 1995, ApJ, 450, 51
Hook I.M., McMahon R.G., Boyle B.J., Irwin M., 1994, MNRAS, 268, 305
Kembhavi A., Feigelson E. D., Singh K. P., 1986, MNRAS, 220, 51
Kollgaard R. I., 1994, Vistas Astron., 38, 29
Komossa S., Fink H. H., 1997, A&A, 327, 555
Large M. I., Mills B. Y., Little A. G., Crawford D. F., Sutton J. M., 1981, MNRAS, 194, 693
La Valley M., Isobe T., Feigelson E. D., 1992, BAAS, 24, 839
Maccacaro T., Gioia I. M., Wolter A., Zamorani G., Stocke J. T., 1988, ApJ, 326, 680
Meyer D. M., Roth K. C., 1990, ApJ, 363, 57
Morrison A., McCammon D., 1983, ApJ, 270, 119
Padovani P., Giommi P., 1995, MNRAS, 277, 1477
Pei Y., Fall M., Bechtold J., 1991, ApJ, 378, 6
Pfeffermann E. et al., 1987, Proc. SPIE, 733, 519
Prieto M. A., 1996, MNRAS, 282, 421
Puchnarewicz E. M., Mason K. O., 1998, MNRAS, 293, 243
Schartel N., 1996, PhD thesis, LMU München
Schartel N., Walter R., Fink H. H., Trümper J., 1996, A&A, 307, 33
Schartel N., Komossa S., Brinkmann W., Fink H. H., Trümper J., Wamsteker W., 1997, A&A, 320, 421
Seaton M. J., 1979, MNRAS, 187, 75P
Siebert J., Brinkmann W., 1998, A&A, 333, 63
Siebert J., Brinkmann W., Morganti R., Tadhunter C. N., Danziger I. J., Fosbury R. A. E., di Serego Alighieri S., 1996, MNRAS, 279, 1331
Srianand R., Kembhavi A., 1997, ApJ, 478, 70
Stickel M., Padovani P., Urry C. M., Fried J. W., Kühr H., 1991, ApJ, 374, 431
Stickel M., Meisenheimer K., Kühr H., 1994, A&AS, 105, 211
Stocke J. T., Morris S. L., Gioia I., Maccacaro T., Schild R., Wolter A., Fleming T. A., Henry J. P., 1991, ApJS, 76, 813
Trümper J., 1982, Adv. Space Res., 2, 241
Turnshek D. A., Wolfe A. M., Lanzetta K. M., Briggs F. H., Cohen R. D., Foltz C. B., Smith H. E., Wilkes B. J., 1989, ApJ, 344, 567
Urry C. M., Padovani P., 1995, PASP, 107, 803
Urry C. M., Sambruna R. M., Worrall D. M., Kollgaard R. I., Feigelson E. D., Perlman E. S., Stocke J. T., 1996, ApJ, 463, 424
Véron-Cetty M.-P., Véron P., 1993, A catalogueue of quasars and active nuclei, 6th edn. ESO Scientific Report No. 13
Voges W., 1992, in Proc. ISY Conference, ESA ISY-3, Space Science, ESA Publications, Noordwijk, p.9
Voges W. et al., 1994, *ROSAT* News, No. 32
Voges W. et al., 1998, A&AS, submitted
Webster R. L., Francis P. J., Peterson B. A., Drinkwater M. J., Masci F. J., 1995, Nat, 375, 469
Wills D., Lynds R., 1978, ApJS, 36, 317
Wright A. E., Otrupcek R. E., 1990, Parkes Catalogue. Australia Telescope National Facility, Epping
Yuan W., Brinkmann W., Siebert J., 1998, A&A, 330, 108
Zimmermann H. U., Becker W., Belloni T., Döbereiner S., Izzo C., Kahabka P., Schwentker O., 1994, MPE Report No. 257

This paper has been typeset from a T_EX/L^AT_EX file prepared by the author.

Downloaded from https://academic.oup.com/mnras/article-abstract/301/1/261/1058213 by Library user on 07 September 2018